A microstructure-based multiscale homogenization model for predicting the elasto-viscoplastic behavior of duplex stainless steels

Eyram Tsekpuia, Adrien Guery, Nathalie Gey, Stéphane Berbenni

A microstructure-based multiscale homogenization model for predicting the elasto-viscoplastic behavior of duplex stainless steels

Eyram Tsekpuia[1], Adrien Guery [2], Nathalie Gey[1], Stéphane Berbenni [1]*

[1]*Université de Lorraine, CNRS, Arts et Métiers ParisTech, LEM3, F-57000 Metz, France*

[2]*EDF Lab Les Renardières, Materials and Mechanics of Components department, F-77818 Moret-sur-Loing, France*

Abstract

Cast duplex austenitic-ferritic (AF) steels are widely used in primary loop of Pressurised Water Reactors (PWR). They offer a good combination of mechanical properties and corrosion resistance. However, at service conditions (about 300°C) and during long times of exposure (more than 10000 h), they are sensitive to thermal aging embrittlement mainly due to the microstructural evolution of ferrite. This is the reason why a good estimate of stresses and strains in the phases are required. To achieve these objectives, different micromechanical models were developed in the past assuming two or three scales in the microstructure. Recent Electron Back-Scatter Diffraction (EBSD) analyses have revealed four scales in the microstructure, which represent the complexity of the microstructure to model, and therefore the main challenge for scale transitions in homogenization models. In the present work, a new microstructure-informed multiscale homogenization scheme is developed. At the first scale, the elastoviscoplastic behavior of single crystals for both phases is modeled using linear elasticity and a viscoplastic crystal plasticity model. An "affine" type formulation based on the first moments of stresses is applied to the inelastic non-linear part of the deformation. Then, at the second scale, an EBSD-informed two-phase austenite/ferrite laminate structure is developed with {110}-type habit planes in ferrite and a Kurdjumov-Sachs orientation relationship (KS-OR) between both phases. At the third scale, the microstructure of the individual primary ferritic grain, the so-called "bicrystal", is then modelled as an aggregate of spherical two-phase laminate structure domains corresponding to the 24 KS-OR variants. The elastoviscoplastic self-consistent scheme (EVPSC) is used through the Translated Fields (TF) homogenization method to obtain the effective behavior at this scale. Here, the same method is applied at the macroscopic scale of an ensemble of primary ferritic grains representing the so-called "poly-bicrystal". At both intermediate scales, EBSD data and analyses are used to physically feed the multiscale model. The results are discussed in terms of local stress/strain responses in ferrite correlated to the different KS-OR variants and habit planes. The effect of primary ferritic grain crystallographic orientation is also studied. Materials parameters corresponding to as received and aged specimen are considered in the discussion of the results.

Keywords: A. Microstructures; EBSD; Homogenization; Crystal plasticity; Duplex steels.

*Corresponding author, E-mail address: Stephane.Berbenni@univ-lorraine.fr

1. Introduction

To understand and predict the mechanical behaviors of multiphase and polycrystalline materials with complex microstructures, advanced micromechanical models need to be developed not only considering macroscopic fields (stresses and strains) but also fields in the different phases. Among these materials, cast duplex stainless steels are widely used in nuclear power plants in the primary loop of the cooling system of pressurized reactors (PWR) due to their good corrosion resistance and their superior mechanical properties (yield stress, ductility) (Solomon and Devine, 1982; Bonnet et al., 1990; Bethmont et al., 1996; Charles, 2009). These two-phase polycrystalline steels are constituted of a α-phase (ferrite) with volume fractions generally varying from 5% to 25% and a γ-phase (austenite). They exhibit a large yield stress due to the presence of body-centered cubic ferrite (b.c.c. crystal structure, the “hard phase”), while ductility is ensured thanks to the presence of face-centered cubic austenite (f.c.c. crystal structure, the “soft phase”). However, during in service behavior at about 300°C and aging during long periods of time (e.g. 10000h), while the mechanical behavior of austenite is not affected, ferrite may exhibit embrittlement and material’s fracture toughness decreases (Bonnet et al., 1990; Devillers-Guerville, 1998; Magnin and Moret, 1982; Trautwein and Gysel, 1982; Le Delliou and Saillet, 2015). Indeed, a spinodal decomposition of the ferrite α-phase (Fe-Cr solid solution) into α'-phase (Cr-rich phase) and α-phase (Fe-rich phase) occurs during aging besides a G-phase precipitation (Auger et al., 1990; Pareige et al., 2015; Badyka et al., 2019). Therefore, the damage mode of ferrite is modified and changes from ductile to brittle fracture due to cleavage cracking. The cleavage mode was observed to be controlled by tensile stresses (Bugat, 2000, Bugat et al. 2001; M’Cirdi, 2000; M'Cirdi et al. 2001). Therefore, good estimates of stresses in both phases and especially in the ferritic phase are needed for as received and aged materials (Bugat, 2000).

Internal stresses in these materials were studied by Verhaeghe et al. (1996) identifying their sources directly from Bauschinger tests for aged and non-aged materials. Damage and fracture mechanisms were studied using TEM by Verhaeghe et al. (1997), X-Ray diffraction methods by M'Cirdi et al. (2001) and SEM with field measurements by Bugat et al. (2001). In a cast aged duplex stainless steel, a crystallographic cleavage criterion, based on a stress normal to a {100} plane in ferrite was reported by M'Cirdi et al. (2001). More recently, in situ synchrotron and neutron diffractions were used to study the evolution of lattice strains in duplex steels during a tensile test and the occurrence of damage in the ferrite (Baczmanski et al. 2016).

New experimental in-situ DIC and EBSD-based methods (Mollens, 2022a,b,c) reveal the heterogeneous deformation and micro-texture complexities, which motivates the development of new EBSD-informed microstructure-based multiscale homogenization model for predicting the elasto-viscoplastic behavior of duplex stainless steels. The microstructure heterogeneities are related to microstructure genesis and local correlations arise due to orientation relationships (OR). For duplex stainless steels, different orientation relationships were reported in the literature (Haghdadi et al., 2018; Mollens et al., 2022b). Most important observed ones are the Kurdjumov-Sachs (KS), Pitsch (P) and Nishiwama-Wassermann (NW). This microstructure genesis can also be simulated by advanced phase field models, considering the KS-OR from ferrite to austenite (Song et al., 2016). From the mechanical ground, full field crystal plasticity models based on Finite Element modeling (CPFEM) are good candidates to predict internal stress and strain fields at the microstructure level of complex microstructures (see e.g. Roters et al., 2010; Dodla et al., 2015; Li et al., 2019; Flipon et al., 2020; Kasemer and Dawson, 2020). However, they are still time consuming for the industrial applications. Homogenization-based models remain relevant, because they are less time consuming but need to be adapted to more complex microstructures than single phase polycrystalline structures using multiple scale transition methods.

Regarding micromechanical mean-field homogenization models for duplex steels, simple approximations using the simple Taylor (1938)'s model were reported by Verhaeghe (1996) and M'Cirdi (2000). The first self-consistent model for two-phase austenite/ferrite steels was due to Weng (1990), who used the Berveiller-Zaoui's (1979) self-consistent model. In this model, ferritic and austenitic grains were supposed to be spherical, which appears to be too simplistic for the present microstructure and isotropic secant moduli were used for proportional loadings only such as tensile loadings. A second numerical model was developed by Sigmund et al. (1995), who also considered a simple modeling assuming an aggregate of both phases with similar shapes. The Berveiller-Zaoui's self-consistent model was also used in combination with a physical intra-granular backstress formulation by Fournier et al. (2011) for predicting the high temperature cyclic behavior of martensitic steels. Baczmanski et al. (2016) used synchrotron and neutron diffraction measurements to calibrate materials parameters in an elasto-plastic self-consistent scheme (EPSC) considering damage in duplex steels.

However, in all these above models, only two scales were considered in the scale transition of the micromechanical model between the phases and the aggregates. Later, Bugat et al. (1999) and Bugat (2000) developed for the first time a 3-scale model for these duplex steels with an intermediate scale called "bi-crystal", which was based on a mean field "Beta model" (see e.g. Cailletaud and Pilvin, 1994; Coudon et al., 2019). This model was developed in isotropic elasticity by Bugat et al.

(1999) and Bugat (2000) and needs to be calibrated with full field FE unit cell calculations. The model was based on the EBSD data acquired in the 2000's, and three different scales were essentially identified (Bugat et al. 1999; Bugat, 2000). Another interesting approach corresponding to multiple scale modeling of the local correlation between phases for purely anisotropic viscoplastic complex microstructures can be found in Lebensohn and Canova (1997), Lebensohn (1999), where the viscoplastic self-sonsistent scheme (VPSC) was extended to consider two-site interactions and lamellar structures in titanium aluminides (TiAl). For the same material, but considering a different modeling approach, Roos et al. (2004) developed a modeling approach based on a three-scale model using the Transformation Field Analysis (TFA) for plasticity together with the elastic self-consistent solution and lamellar phases. Kowalczyk-Gajewska (2011) developed a micromechanical model of polycrystalline materials with lamellar substructure in the framework of the Hill's EPSC model (Hill, 1965) to study the elastic anisotropies and the initial yield surfaces for polycrystalline microstructures of Ti-Al. Franciosi and Berbenni (2008) also developed a multi-scale sequential multi-laminate model based on a non-uniform TFA approach with affine approximation to describe the evolution of heterogeneous plastic domains in metallic polycrystals. Stress/strain estimates were improved at the macroscopic and at the grain levels, as compared to classic EPSC scheme, which assumes piece-wise uniform plastic strains in grains. The lamellar-based approach of Lebensohn et al. (1997,1999) was recently applied to a Ti-6Al-4V alloy to accurately model the local crystallographic correlations in such complex multiscale microstructures (Riyad et al., 2021).

Therefore, we propose to extend the EVPSC (Elasto-Visco-Plastic Self-Consistent) scheme based on the "Translated Field" (TF) method with affine linearization of the viscoplastic flow rule as developed by Mareau and Berbenni (2015) for such duplex steels complex microstructure. This advanced EVPSC scheme was successfully applied to near-β titanium alloys in Lahdi et al. (2018, 2020). While the original approach of Paquin et al. (1999, 2001) was derived from a classical secant approximation, this work adopts the first order affine linearization (see e.g. Masson et al., 2000; Doghri et al., 2010) of the viscoplastic flow rule, i.e. a first order Taylor expansion of the viscoplastic strain rate at the local scale. It has been observed in Mareau and Berbenni (2015) that the first order affine formulation yields softer responses than the secant formulation for different elastoviscoplastic polycrystals during monotonous and cyclic loadings. Other EVPSC approaches using the "additive interaction law" (Molinari et al., 1997; Mercier and Molinari, 2009) were adapted for polycrystals with "affine"-type approximation at large strains (Wang et al., 2010; Zecevic et al. 2020). Another efficient EVPSC scheme was also derived by Jeong and Tomé (2020) and applied to steels subjected to loading path changes. According to Mercier et al. (2012), Berbenni and Capolungo (2015) and Mareau and Berbenni (2015), the use of the first order affine formulation improves the estimate of the effective behavior, in comparisons with full-field calculations (FEM, FFT), even when the

viscoplastic flow rule is highly nonlinear. Homogenization methods for elastoviscoplastic composite materials considering field statistics, i.e. second moments of stresses, were derived (see e.g. Lahellec and Suquet, 2007, 2013; Brassart et al., 2012; Wu et al., 2017; Masson et al., 2020; Berbenni, 2021). A recent modeling approach for elastoviscoplastic polycrystals based on a differential variational procedure (Das and Ponte Castañeda, 2020) further improves the numerical results compared to FFT full field results. However, it needs a more complex numerical treatment of cyclic and non-proportional loadings, which has not been solved yet.

Following the recent findings and EBSD analyses of Mollens et al. (2022b), it seems nowadays that four relevant scales shall be considered when dealing with the complex microstructure of austenito-ferritic (duplex) steels. The “microscale” is defined as the one the single heterogeneities in the material. In this case, the single crystalline austenite lath or the single crystalline ferrite interlayer is considered at the microscale and classic crystal plasticity framework will be used to describe the small strain elastoviscoplastic behavior of both phases. The second scale is dictated by an austenite lath cluster characterized by constrained morphological and crystallographic parameters. The treatment of this specific intermediate scale, here called “mesoscale”, will need an extension of the classic EVPSC scheme using a double scale transition starting from a laminate structure (LS) that will be identified from EBSD analysis and considering all the possible 24 KS-OR variants in the modeling. The third scale is defined by the primary ferritic grain that contains all the austenite lath clusters. It will be called a “bi-crystal”. Finally, the fourth scale is defined as an aggregate of primary ferritic grains and will be called a “poly-bi-crystal” in the manuscript. For both “bi-crystal” and “poly-bicrystal” modeling, the EVPSC scheme will be used as transition rule from “mesoscale” to “macroscale 1” and “macroscale 2”, respectively. The crystal plasticity parameters of the model will be calibrated at “macroscale 2” from experimental tensile curves.

The paper is organized as follows. In section 2, the duplex stainless steel is presented. The chemical composition, the microstructure and the tensile mechanical properties are reported. In addition, an EBSD analysis is proposed to identify the different variants and the heterogeneities in the microstructure. In section 3, the micromechanical model based on a multiscale homogenization method for elastoviscoplastic heterogeneous materials is developed and specifically applied to duplex stainless steels. In section 4, the results of the model are presented at different scales (meso-scale, macro-scale) and the strain/stress fields in both phases are predicted for the different KS-OR variants present in the primary ferritic grains. The effects of ferrite grain orientations and aging are numerically studied. The different internal stresses present in the microstructure are analyzed in the light of this new approach through cyclic loading responses.

2. Material

2.1. Microstructure and mechanical properties

The material of interest is a CF8M alloy (AFNOR Z3CND1910), which is representative of cast duplex stainless steels used in the primary loop components of Pressurized Water Reactors (PWR) in France. Its chemical composition is given in Table 1. Its microstructure has been characterized by EBSD in the previous study of Mollens (2022a), see Figure 1. It is made of primary polygonal ferritic grains of 200 to 1000 micrometers partially transformed with respect of an orientation relationship into Widmanstätten austenite laths of 10 to 50 micrometers width. The retained ferrite phase accounts for about 25% of the total volume fraction. It is located between the austenite laths. Here, only the cast microstructure will be thoroughly modeled, but we will discuss the prospective effect of aging by considering a higher flow stress for ferrite, which may be due to precipitation during aging.

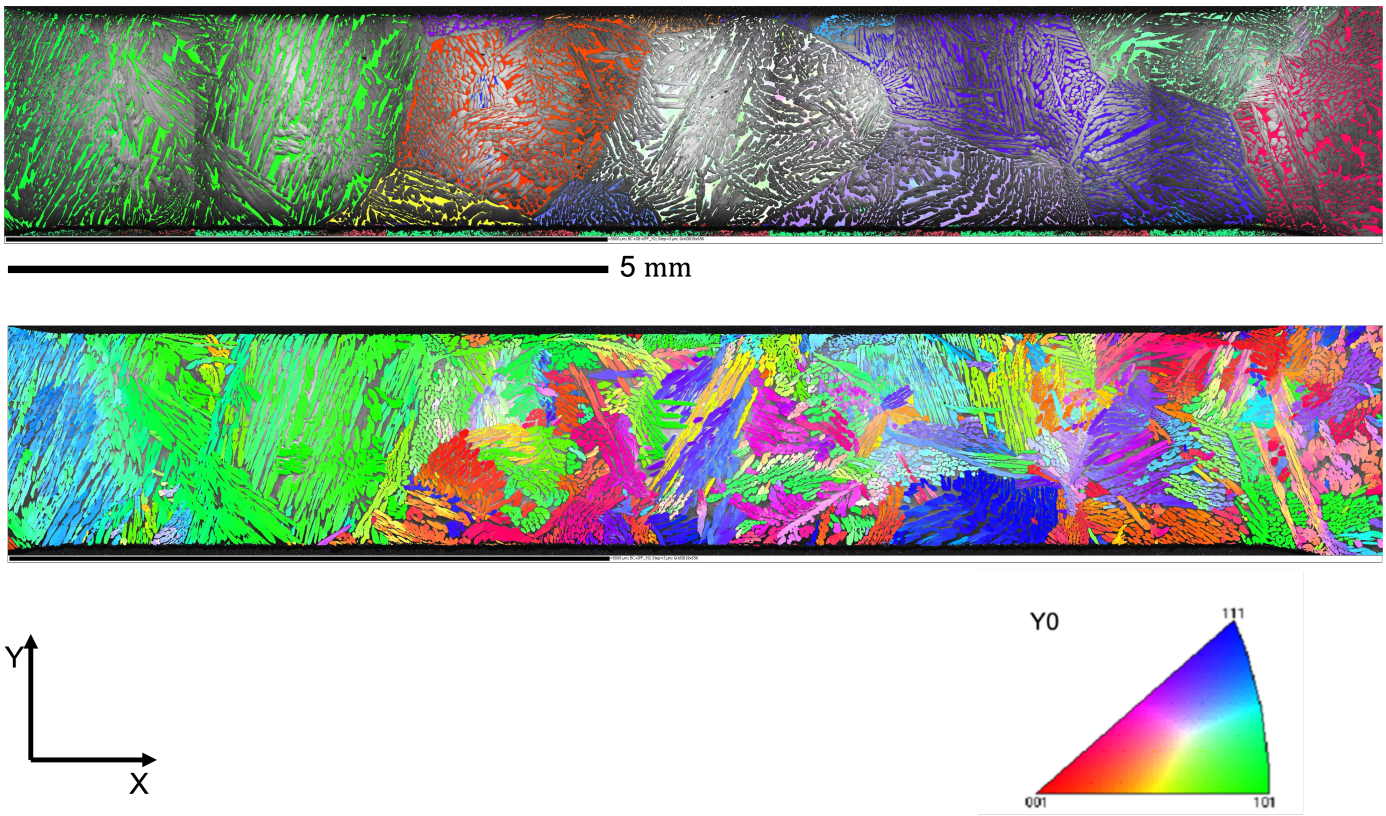

Figure 1: Inverse Pole Figure map//Y of the as-cast duplex steel respectively for retained ferrite (upper map) and austenite (bottom map) using EBSD data from Mollens (2022a).

Table 1. Chemical composition of the studied CF8M material from Mollens (2022c).

Element	C	Mn	Si	Ni	Cr	Mo	S	P
Content (%wt)	0.032	0.80	1.04	10.4	20.9	2.68	0.0007	0.025

The mechanical behavior of the material at the as-received state and after thermal aging at 350°C during 1000h has been characterized by Mollens (2022a) with tensile tests using normalized TC6 specimens. The resulting tensile curves are shown in Figure 2. Thermal aging induces a small increase of the yield stress, an increase of the ultimate tensile stress and a decrease of the elongation at fracture, consistent with previous studies (Bugat, 2000; Michaud et al.; 1994).

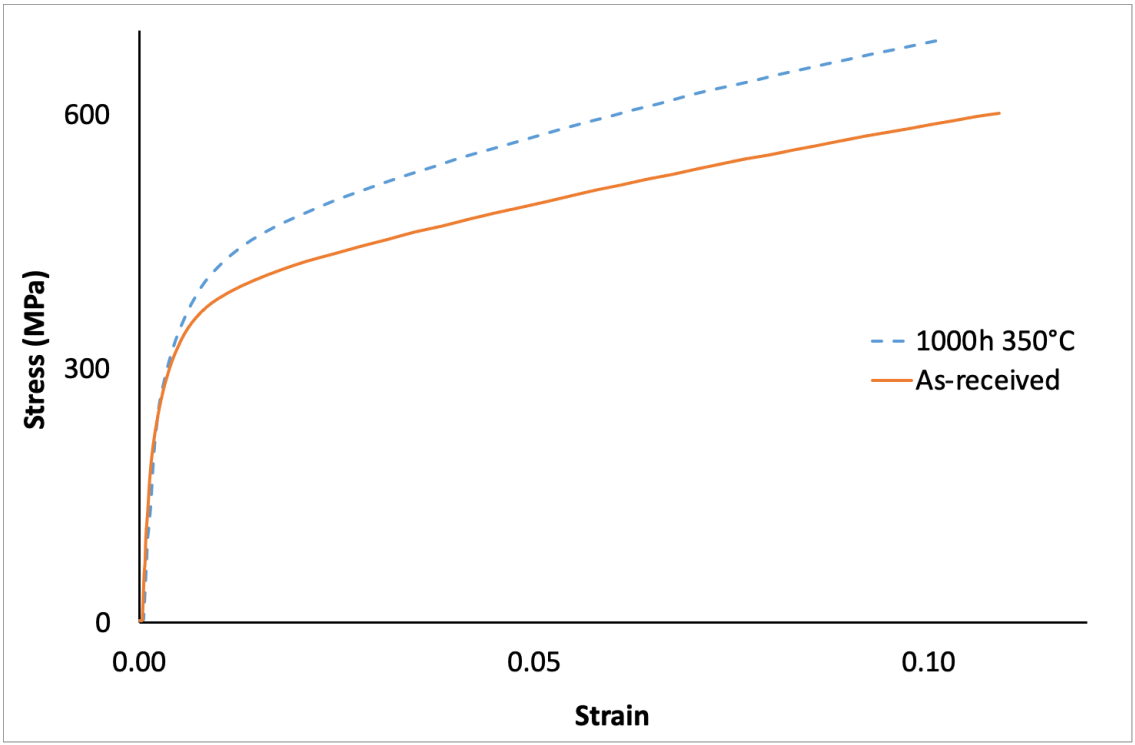

Figure 2: Tensile behavior measured at ambient temperature on the studied material at the as-received state and aged 1000h at 350°C (Mollens, 2022a).

2.2. Crystallographic features of the microstructure and resulting scales

EBSD data shown in Figure 1 were first analyzed to characterize the local orientation correlations between both ferrite/austenite phases. Figure 3 displays the local deviation from KS-OR at the ferrite/austenite interfaces. The duplex microstructure was found to display a significantly higher content of close KS-OR interfaces, which are represented with white and yellow interfaces in Figure 3. However, no unique and strict orientation relationship exist between both phases, as already mentioned in previous work (Mollens, 2022b). Moreover, close to some primary ferrite boundaries, the austenite phase exhibit no longer a lath-like morphology and no OR is observed. This happens mainly for austenite phase that have grown at each side of a primary ferrite grain with close orientation.

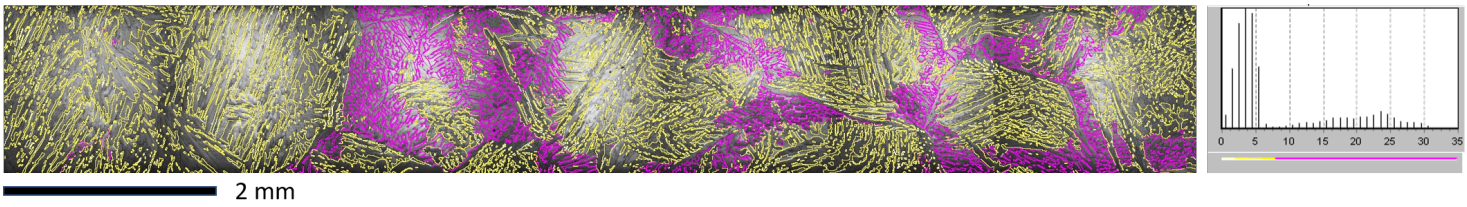

Figure 3: EBSD map plotting the K-S OR deviation at the ferrite/austenite interfaces and the corresponding distribution with the angular deviation color code (as received cast material).

The EBSD data were further investigated to analyze the trace of ferrite/austenite interfaces respecting KS-OR. The result shows that most of the traces are consistent with a {110}α plane of the primary ferrite grain, which acts as Habit Plane (denoted HP in the following) in the reverse KS -OR (see an example in Figure 4).

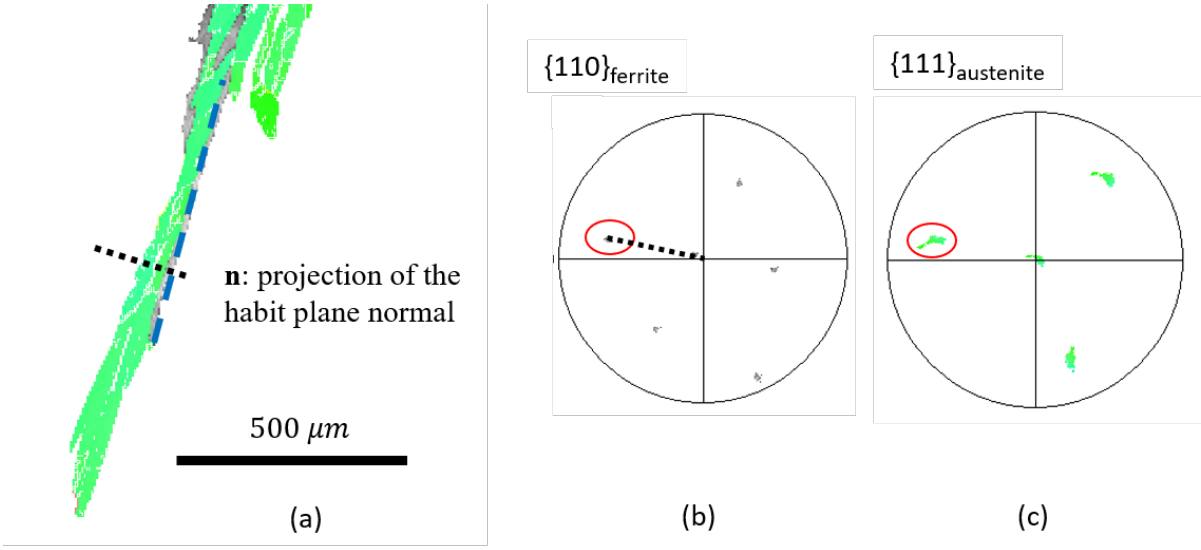

Figure 4: (a) Geometric definition of the habit plane with habit plane normal **n**, (b) {110} pole figure for ferrite, (c) {111} pole figure for austenite.

Assuming close KS-OR for the ferrite to austenite transformation, Table 2 gives the 24 potential variants obtained from a primary ferrite grain (defined by the orientation (0,0,0) for ferrite). For each variant, the corresponding HP is indicated as well as the Bain group it belongs to. Packets of 4 variants sharing the same HP are identified by a similar color. Inside such a packet, the 4 variants belong 2 by 2 to two Bain domains.

Table 2. 24 KS variant definition for b.c.c. to f.c.c transformation according to the KS-OR. Color code means the HP's type (6 different habit planes). The variants are divided into 3 Bain groups, denoted B1 to B3. The list of the 24 group symmetry matrices to generate these variants is given in Table A.2, see Appendix.

Variants	φ_1 (°)	ϕ (°)	φ_2 (°)	HP plane (h k l)	HP direction [u v w]	HP name	Bain group
V1	5.77	48.19	5.77	$(1\ \bar{1}\ 0)$	$[1\ 1\ 1]$	H1	B1:x
V2	95.77	48.19	5.77	$(1\ 1\ 0)$	$[\bar{1}\ 1\ 1]$	H2	B2:y
V3:	185.77	48.19	5.77	$(\bar{1}\ 1\ 0)$	$[\bar{1}\ \bar{1}\ 1]$	H1	B1:x
V4:	275.77	48.19	5.77	$(\bar{1}\ \bar{1}\ 0)$	$[1\ \bar{1}\ 1]$	H2	B2:y
V5:	6.41	137.87	14.39	$(1\ 0\ \bar{1})$	$[1\ \bar{1}\ 1]$	H3	B1:x
V6:	48.05	85.70	99.62	$(1\ 0\ 1)$	$[\bar{1}\ \bar{1}\ 1]$	H4	B3:z
V7:	353.59	42.13	194.39	$(\bar{1}\ 0\ 1)$	$[\bar{1}\ \bar{1}\ \bar{1}]$	H3	B1:x
V8:	311.95	94.30	279.62	$(\bar{1}\ 0\ \bar{1})$	$[1\ \bar{1}\ \bar{1}$	H4	B3:z
V9:	96.41	137.87	14.39	$(0\ 1\ \bar{1})$	$[1\ 1\ 1]$	H5	B2:y
V10:	138.05	85.70	99.62	$(0\ 1\ 1)$	$[1\ \bar{1}\ 1]$	H6	B3:z
V11:	83.59	42.13	194.39	$(0\ \bar{1}\ 1)$	$[1\ \bar{1}\ \bar{1}]$	H5	B2:y
V12:	41.95	94.30	279.62	$(0\ \bar{1}\ \bar{1})$	$[1\ 1\ \bar{1}]$	H6	B3:z
V13:	186.41	137.87	14.39	$(\bar{1}\ 0\ \bar{1})$	$[\bar{1}\ 1\ 1]$	H4	B1:x
V14:	228.05	85.70	99.62	$(\bar{1}\ 0\ 1)$	$[1\ 1\ 1]$	H3	B3:z
V15:	173.59	42.13	194.39	$(1\ 0\ 1)$	$[1\ 1\ \bar{1}]$	H4	B1:x
V16:	131.95	94.30	279.62	$(1\ 0\ \bar{1})$	$[\bar{1}\ 1\ \bar{1}]$	H3	B3:z
V17:	276.41	137.87	14.39	$(0\ \bar{1}\ \bar{1})$	$[\bar{1}\ \bar{1}\ 1]$	H6	B2:y
V18:	318.05	85.70	99.62	$(0\ \bar{1}\ 1)$	$[\bar{1}\ 1\ 1]$	H5	B3:z
V19:	263.59	42.13	194.39	$(0\ 1\ 1)$	$[\bar{1}\ 1\ \bar{1}]$	H6	B2:y
V20:	221.95	94.30	279.62	$(0\ 1\ \bar{1})$	$[\bar{1}\ \bar{1}\ \bar{1}]$	H5	B3:z
V21:	174.23	131.81	185.77	$(1\ 1\ 0)$	$[1\ \bar{1}\ \bar{1}]$	H2	B1:x
V22:	264.23	131.81	185.77	$(\bar{1}\ 1\ 0)$	$[1\ 1\ \bar{1}]$	H1	B2:y
V23:	354.23	131.81	185.77	$(\bar{1}\ \bar{1}\ 0)$	$[\bar{1}\ 1\ \bar{1}]$	H2	B1:x
V24:	84.23	131.81	185.77	$(1\ \bar{1}\ 0)$	$[\bar{1}\ \bar{1}\ \bar{1}]$	H1	B2:y

Finally, from the analysis of the experimental EBSD data, 4 scales can be identified to describe the complex microstructure of the as received cast duplex steel (see Figure 5). The first scale (microscale) is given by the austenite lath characterized by a smooth orientation spread. This lath results from a displacive transformation according to a close {110}α HP and respecting closely the KS-OR with the surrounding ferrite grain. Cluster of adjacent austenite laths often share the same orientation with an increased orientation spread. They are separated by layers of primary ferrite. This cluster is called the “two-phase laminate structure” (LS) and corresponds to the second scale (mesoscale) of the duplex microstructure. The third scale is given by the primary ferrite grain, that includes different two-phase LS, which means different austenite laths of different morphological and crystallographic orientations (variants). It is called “bicrystal”. One can notice that adjacent LS often include two austenite variants belonging to the same Bain group. Finally, the last scale (macroscale 2) defines the whole microstructure covering different primary ferrite grains. It is called “poly-bicrystal”.

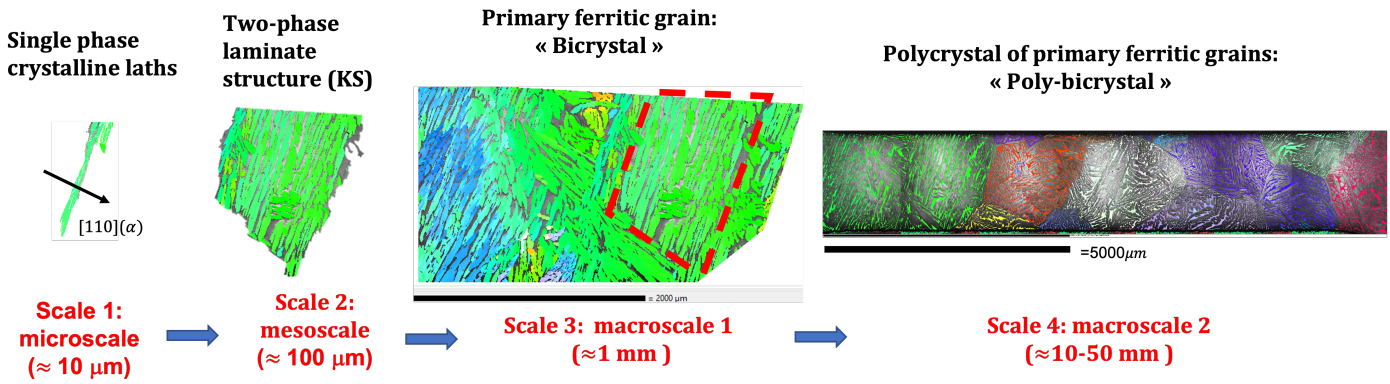

Figure 5: Multiscale description of the microstructure.

3. Multiscale homogenization model

The modeling of the elastoviscoplastic behavior of duplex stainless steels is derived following the different scales reported in Figure 5. The TF-based EVPSC model is reconsidered with two homogenization steps (see Figure 6). The first step is a homogenization procedure for the two-phase (ferrite/austenite) LS considering an elastoviscoplastic framework with "affine"-type formulation for both phases. Stress/strain concentration equations allow to give an estimate of mean fields in both phases accounting for the stress/strain incompatibilities due to the presence of the HP. The homogenized properties of the LS obtained at this first step (mesoscale model) will be incorporated in the EVPSC scheme for the second homogenization procedure. This one considers an ensemble of two-phase LS constrained by spherical domains corresponding to the different KS-OR variants. The 24 variants (see Table 2) will be considered with equal volume fraction for each primary ferritic grain. Then, the macroscale model is built up with the homogenized elastoviscoplastic behavior for one primary ferritic grain (the so-called "bicrystal") or the 15 ones reported in Table A.1 in the Appendix (the so-called "poly-bicrystal"). In the following, the model is constituted of four pillars: the elastoviscoplastic framework with "affine"-type formulation is reported in section 3.1. Then, the macroscale model is first derived using the TF-EVPSC model in section 3.2. All the equations of the mesoscale model based on the LS needed to be transferred to the macroscale model is detailed in section 3.3. Finally, the constitutive laws for austenite and ferrite at the single crystalline level are given in section 3.4.

Throughout the development of the model, bold characters are used to define rank 2 and 4 tensors in vector notations, ":" denotes the contracted product between 2 tensors. The symbols $\langle\cdot\rangle$ and $\langle\cdot\rangle^L$ denote the ensemble volume averages at the macroscale and the mesoscale, respectively. Indicial notations are used using Cartesian coordinates with the Einstein's summation convention.

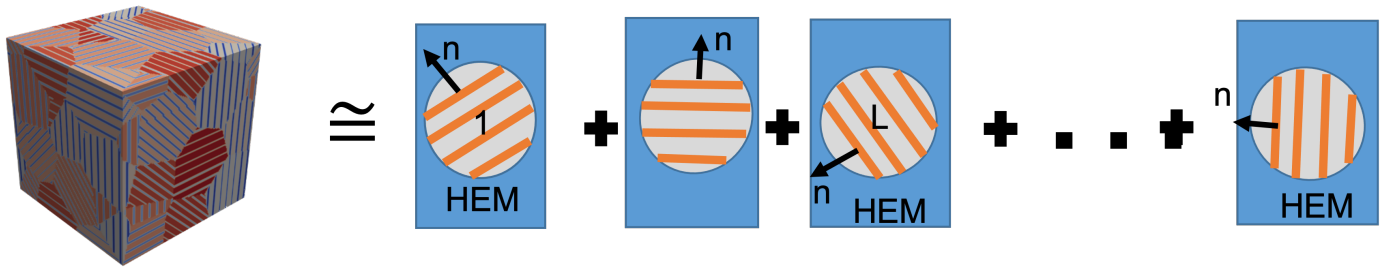

Figure 6: Schematic principle of the multiscale modeling based on two scale transitions. The first one is the transition from micro- to meso-scales for the homogenization of two-phase austenite/ferrite LS (the grey color represents austenite laths and the orange color represents ferrite interlayers). The second one is the transition from meso- to macro-scales to derive the HEM (Homogeneous Equivalent Medium)'s behavior at the macroscale (blue color).

3.1. Elastoviscoplastic framework and "affine"-type formulation

Within the infinitesimal strain framework, the total local strain rate relative to an elasto-viscoplastic behavior (of Maxwell type) is decomposed into:

$$\dot{\boldsymbol{\varepsilon}} = \dot{\boldsymbol{\varepsilon}}^{e} + \dot{\boldsymbol{\varepsilon}}^{vp} \tag{1}$$

with $\dot{\boldsymbol{\varepsilon}}^{\mathbf{e}} = \mathbf{s}:\dot{\boldsymbol{\sigma}}$ from the generalized Hooke's law where $\mathbf{s}$ $(= \mathbf{c}^{-1})$ is the local elastic compliance tensor, and $\dot{\boldsymbol{\varepsilon}}^{\mathbf{vp}} = \mathbf{g}(\boldsymbol{\sigma})$ is the nonlinear viscoplastic constitutive law (plastic flow rule) dependent on the Cauchy stress tensor $\boldsymbol{\sigma}$. It will be determined from the constitutve laws of single crystalline laths for both austenite and ferrite (see section 3.4). As performed in Mareau and Berbenni (2015), its first order "affine" linearization can be written as follows at a given reference stress:

$$\dot{\boldsymbol{\varepsilon}}^{vp} = \boldsymbol{g}(\boldsymbol{\sigma}) \approx \boldsymbol{m}_{\boldsymbol{t}}:\boldsymbol{\sigma} + \dot{\boldsymbol{\eta}} \tag{2}$$

where $\mathbf{m_t}$ (respectively $\mathbf{b_t} = \mathbf{m_t}^{-1}$) is the tangent viscoplastic compliance tensor (respectively the tangent viscoplastic modulus tensor) defined by:

$$\boldsymbol{m}_{\boldsymbol{t}} = \frac{\partial \boldsymbol{g}(\boldsymbol{\sigma})}{\partial \boldsymbol{\sigma}} \tag{3}$$

$\dot{\boldsymbol{\eta}}$ corresponds to the back-extrapolated viscoplastic strain rate tensor. The Cauchy stress tensor can also be expressed as a nonlinear function $\mathbf{h}$ of $\dot{\boldsymbol{\varepsilon}}^{\mathbf{vp}}$ and then could be written in its linearized form at a given reference viscoplastic strain rate as:

$$\boldsymbol{\sigma} = \boldsymbol{h}(\dot{\boldsymbol{\varepsilon}}^{vp}) \approx \boldsymbol{b_t}\!:\dot{\boldsymbol{\varepsilon}}^{vp} + \boldsymbol{\zeta} \quad (4)$$

$\boldsymbol{\zeta}$ is the back-extrapolated stress tensor related to the back-extrapolated viscoplastic strain rate by $\boldsymbol{\zeta} = -\mathbf{b_t}\!:\dot{\boldsymbol{\eta}}$. Therefore, the final linearized form of the elastoviscoplastic constitutive law is:

$$\dot{\boldsymbol{\varepsilon}} = \boldsymbol{s}\!:\dot{\boldsymbol{\sigma}} + \boldsymbol{m_t}\!:\boldsymbol{\sigma} + \dot{\boldsymbol{\eta}} \quad (5)$$

3.2. Macroscale model: EVPSC

3.2.1. Schematic principle and macroscopic averages

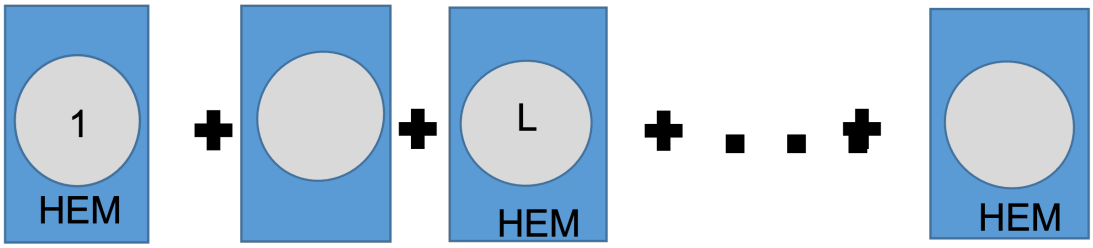

Figure 7: Schematic principle of the macroscale model (TF-EVPSC) with LS: Translated Field (TF) based elasto-visco-plastic self-consistent (EVPSC) model with homogenized LS in grey color.

In this paper, the scale transition from a single two-phase LS to "bi-crystal" or "poly-bicrystal" is assessed through the TF-EVPSC method with affine-type extension. This TF-EVPSC scheme was first developed in Mareau and Berbenni (2015) and more recently applied to polycrystalline β-Ti alloys by Lahdi et al. (2018,2020). For each laminate denoted "L", the elastic strain rate is given by the linear elastic Hooke's law: $\dot{\boldsymbol{\varepsilon}}^{e\,L} = \boldsymbol{s}^{L} : \dot{\boldsymbol{\sigma}}^{L}$, and, the viscoplastic strain rate is formulated using an affine-type approximation of the viscoplastic strain rate: $\dot{\boldsymbol{\varepsilon}}^{vp\,L} \approx \boldsymbol{m_t}^{L} : \boldsymbol{\sigma}^{L} + \dot{\boldsymbol{\eta}}^{L}$, or, $\boldsymbol{\sigma}^{L} \approx \boldsymbol{b_t}^{L}\!:\dot{\boldsymbol{\varepsilon}}^{vp\,L} + \boldsymbol{\zeta}^{L}$, see equations (2-5).

3.2.2. *Strain and stress concentration equations*

In the TF-EVPSC, the strain rate concentration law is obtained at the level of each LS (here "L" is used to denote the averaged fields on one LS) following Mareau and Berbenni (2015) and Lhadi et al. (2018):

$$\dot{\boldsymbol{\varepsilon}}^{L} = \langle\dot{\boldsymbol{\varepsilon}}\rangle^{L} = \boldsymbol{A}^{C}\!:\dot{\boldsymbol{E}} + \boldsymbol{A}^{C}\!:\boldsymbol{\Gamma}_{l}^{B_t}\!:\left(\boldsymbol{b}_{t}^{\,L}\!:\dot{\boldsymbol{\eta}}^{L} + \boldsymbol{B}_{t}^{e}\!:\dot{\boldsymbol{N}}^{e}\right) + \boldsymbol{A}^{C}\!:\boldsymbol{\Gamma}_{l}^{C}\!:\left(\boldsymbol{\delta c}^{L}\!:\dot{\boldsymbol{\varepsilon}}^{vp\,L} + \boldsymbol{c}^{L}\!:\boldsymbol{A}^{C}\!:\left(\langle\dot{\boldsymbol{\varepsilon}}^{vp}\rangle - \dot{\boldsymbol{E}}^{vp,e}\right)\right) -$$
$$\boldsymbol{A}^{C}\!:\boldsymbol{\Gamma}_{l}^{B_t}\!:\left(\boldsymbol{\delta b}_{t}^{\,L}\!:\dot{\boldsymbol{\varepsilon}}^{vpL} - \boldsymbol{b}_{t}^{\,L}\!:\boldsymbol{A}^{B_t}\!:\left(\boldsymbol{M}_{t}^{e}\!:\boldsymbol{\Sigma} + \dot{\boldsymbol{N}}^{e} - \langle\dot{\boldsymbol{\varepsilon}}^{vp}\rangle\right)\right) + \boldsymbol{A}^{C}\!:\left(\boldsymbol{\Gamma}_{l}^{C}\!:\boldsymbol{C}^{e} - \boldsymbol{\Gamma}_{l}^{B_t}\!:\boldsymbol{B}_{t}^{e}\right)\!:\left(\dot{\boldsymbol{\varepsilon}}^{vpL} - \boldsymbol{A}^{B_t}\!:\langle\dot{\boldsymbol{\varepsilon}}^{vp}\rangle\right) -$$
$$\boldsymbol{A}^{C}\!:\left(\boldsymbol{\Gamma}_{l}^{C}\!:\boldsymbol{C}^{e} - \boldsymbol{\Gamma}_{l}^{B_t}\!:\boldsymbol{B}_{t}^{e}\right)\!:\left(\boldsymbol{A}^{B_t}\!:\boldsymbol{\Gamma}_{l}^{B_t}\!:\left(\boldsymbol{b}_{t}^{\,L}\!:\dot{\boldsymbol{\eta}}^{L} - \boldsymbol{B}_{t}^{e}\!:\dot{\boldsymbol{N}}^{e}\right)\right) \qquad (6)$$

where the Eshelby tensors (Eshelby, 1957) associated to $\boldsymbol{C}^{e}$ and $\boldsymbol{B}_{t}^{e}$ are given by $\boldsymbol{\Gamma}_{l}^{C}\!:\boldsymbol{C}^{e}, \boldsymbol{\Gamma}_{l}^{B_t}\!:\boldsymbol{B}_{t}^{e}$ respectively with $\boldsymbol{\Gamma}_{\mathbf{l}}^{\mathbf{C\ or\ B_t}}$ the local parts of the modified Green operators (Kröner, 1990). In this equation, $\dot{\boldsymbol{E}}$ is the applied strain rate tensor. The 4th rank elastic and viscoplastic strain concentrations tensors $\boldsymbol{A}^{C}$ and $\boldsymbol{A}^{B_t}$ are defined as $\boldsymbol{A}^{C} = \left(\boldsymbol{I} + \boldsymbol{\Gamma}_{l}^{C}\!:\boldsymbol{\delta c}^{L}\right)^{-1}$ and $\boldsymbol{A}^{B_t} = \left(\boldsymbol{I} + \boldsymbol{\Gamma}_{l}^{B_t}\!:\boldsymbol{\delta b}_{t}^{\,L}\right)^{-1}$ respectively, with $\boldsymbol{I}$ the fourth order unit tensor, and $\boldsymbol{\delta b}_{t}^{\,L} = \boldsymbol{b}_{t}^{\,L} - \boldsymbol{B}_{t}^{e}$ and $\boldsymbol{\delta c}^{L} = \boldsymbol{c}^{L} - \boldsymbol{C}^{e}$. The effective elastic and viscoplastic moduli, $\boldsymbol{C}^{e}$ and $\boldsymbol{B}_{t}^{e}$, are given by the 1-site SC scheme iteration loops with a fixed-point algorithm:

$$\boldsymbol{C}^{e} = \langle\boldsymbol{c}^{L}\!:\boldsymbol{A}^{C}\rangle\!:\langle\boldsymbol{A}^{C}\rangle^{-1} \qquad (7a)$$

$$\boldsymbol{B}_{t}^{e} = \langle\boldsymbol{b}_{t}^{\,L}\!:\boldsymbol{A}^{B_t}\rangle\!:\langle\boldsymbol{A}^{B_t}\rangle^{-1} \qquad (7b)$$

The effective back-extrapolated strain rate $\dot{\boldsymbol{N}}^{e}$ in equation (6) is obtained from:

$$\boldsymbol{B}_{t}^{e}\!:\dot{\boldsymbol{N}}^{e} = \langle\boldsymbol{b}_{t}^{\,L}\!:\dot{\boldsymbol{\eta}}^{L} - \boldsymbol{b}_{t}^{\,L}\!:\boldsymbol{A}^{B_t}\!:\boldsymbol{\Gamma}_{l}^{B_t}\!:\left(\boldsymbol{b}_{t}^{\,L}\!:\dot{\boldsymbol{\eta}}^{L} - \boldsymbol{B}_{t}^{e}\!:\dot{\boldsymbol{N}}^{e}\right)\rangle \qquad (8)$$

then:

$$\dot{\boldsymbol{N}}^{e} = \boldsymbol{M}_{t}^{e}\!:\left(\langle\boldsymbol{b}_{t}^{\,L}\!:\boldsymbol{A}^{B_t}\!:\boldsymbol{\Gamma}_{l}^{B_t}\rangle - \boldsymbol{I}\right)^{-1}\!:\langle\boldsymbol{b}_{t}^{\,L}\!:\boldsymbol{A}^{B_t}\!:\boldsymbol{\Gamma}_{l}^{B_t}\!:\boldsymbol{b}_{t}^{\,L}\!:\dot{\boldsymbol{\eta}}^{L} - \boldsymbol{b}_{t}^{\,L}\!:\dot{\boldsymbol{\eta}}^{L}\rangle \qquad (9)$$

Substituting the strain rate equation (6) in the local constitutive law gives the stress rate in each laminate "L":

$$\dot{\boldsymbol{\sigma}}^{L} = \langle\dot{\boldsymbol{\sigma}}\rangle^{L} = \boldsymbol{c}^{L}\!:\boldsymbol{A}^{C}\!:\left(\boldsymbol{S}^{e}\!:\dot{\boldsymbol{\Sigma}} + \dot{\boldsymbol{E}}^{vp,e}\right) - \boldsymbol{c}^{L}\!:\dot{\boldsymbol{\varepsilon}}^{vpL} + \boldsymbol{c}\!:\boldsymbol{A}^{C}\!:\boldsymbol{\Gamma}_{l}^{B_t}\!:\left(\boldsymbol{b}_{t}^{\,L}\!:\dot{\boldsymbol{\eta}}^{L} + \boldsymbol{B}_{t}^{e}\!:\dot{\boldsymbol{N}}^{e}\right) + \boldsymbol{c}^{L}\!:\boldsymbol{A}^{C}\!:\boldsymbol{\Gamma}_{l}^{C}\!:(\boldsymbol{\delta c}^{L}\!:\dot{\boldsymbol{\varepsilon}}^{vpL} +$$
$$\boldsymbol{c}^{L}\!:\boldsymbol{A}^{C}\!:\left(\langle\dot{\boldsymbol{\varepsilon}}^{vp}\rangle - \dot{\boldsymbol{E}}^{vp,e}\right)) - \boldsymbol{c}^{L}\!:\boldsymbol{A}^{C}\!:\boldsymbol{\Gamma}_{l}^{B_t}\!:\left(\boldsymbol{\delta b}_{t}^{\,L}\!:\dot{\boldsymbol{\varepsilon}}^{vpL} - \boldsymbol{b}_{t}\!:\boldsymbol{A}^{B_t}\!:\left(\boldsymbol{M}_{t}^{e}\!:\boldsymbol{\Sigma} + \dot{\boldsymbol{N}}^{e} - \langle\dot{\boldsymbol{\varepsilon}}^{vp}\rangle\right)\right) + \boldsymbol{c}^{L}\!:\boldsymbol{A}^{C}\!:\left(\boldsymbol{\Gamma}_{l}^{C}\!:\boldsymbol{C}^{e} -$$
$$\boldsymbol{\Gamma}_{l}^{B_t}\!:\boldsymbol{B}_{t}^{e}\right)\!:\left(\dot{\boldsymbol{\varepsilon}}^{vpL} - \boldsymbol{A}^{B_t}\!:\langle\dot{\boldsymbol{\varepsilon}}^{vp}\rangle\right) - \boldsymbol{c}^{L}\!:\boldsymbol{A}^{C}\!:\left(\boldsymbol{\Gamma}_{l}^{C}\!:\boldsymbol{C}^{e} - \boldsymbol{\Gamma}_{l}^{B_t}\!:\boldsymbol{B}_{t}^{e}\right)\!:\left(\boldsymbol{A}^{B_t}\!:\boldsymbol{\Gamma}_{l}^{B_t}\!:\left(\boldsymbol{b}_{t}^{\,L}\!:\dot{\boldsymbol{\eta}}^{L} - \boldsymbol{B}_{t}^{e}\!:\dot{\boldsymbol{N}}^{e}\right)\right) \qquad (10)$$

3.2.3. Macroscopic behavior

The effective properties obtained from the averaging equations of homogenization theory ($\langle\dot{\boldsymbol{\varepsilon}}\rangle = \dot{\mathbf{E}}$, $\langle\dot{\boldsymbol{\sigma}}\rangle = \dot{\boldsymbol{\Sigma}}$ and $\langle\boldsymbol{\sigma}\rangle = \boldsymbol{\Sigma}$). The macroscopic effective behavior is given by: $\dot{\boldsymbol{E}} = \boldsymbol{S}^{e}\!:\dot{\boldsymbol{\Sigma}} + \dot{\boldsymbol{E}}^{vp,e}$, where the effective viscoplastic strain rate $\dot{\boldsymbol{E}}^{vp,e}$ which is chosen to impose the macrohomogeneity condition $\langle\dot{\boldsymbol{\sigma}}\rangle = \dot{\boldsymbol{\Sigma}}$ is obtained as follows:

$$
\begin{aligned}
\dot{\boldsymbol{E}}^{vp,e} = \boldsymbol{Z}:\langle \boldsymbol{c}^{\boldsymbol{L}}:\dot{\boldsymbol{\varepsilon}}^{vp\boldsymbol{L}}\rangle - \boldsymbol{Z}:\langle \boldsymbol{c}^{\boldsymbol{L}}:\boldsymbol{A}^{\boldsymbol{C}}:\boldsymbol{\Gamma}_{\boldsymbol{l}}^{\boldsymbol{B}_t}:\left(\boldsymbol{b}_{\boldsymbol{t}}{}^{\boldsymbol{L}}:\dot{\boldsymbol{\eta}}^{\boldsymbol{L}} - \boldsymbol{B}_{\boldsymbol{t}}^{\boldsymbol{e}}:\dot{\boldsymbol{N}}^{\boldsymbol{e}}\right)\rangle \\
- \boldsymbol{Z}:\langle \boldsymbol{c}^{\boldsymbol{L}}:\boldsymbol{A}^{\boldsymbol{C}}:\boldsymbol{\Gamma}_{\boldsymbol{l}}^{\boldsymbol{C}}:\left(\boldsymbol{\delta c}^{\boldsymbol{L}}:\dot{\boldsymbol{\varepsilon}}^{vp\boldsymbol{L}} + \boldsymbol{c}^{\boldsymbol{L}}:\boldsymbol{A}^{\boldsymbol{C}}:\langle\dot{\boldsymbol{\varepsilon}}^{vp}\rangle\right)\rangle \\
+ \boldsymbol{Z}:\langle \boldsymbol{c}^{\boldsymbol{L}}:\boldsymbol{A}^{\boldsymbol{C}}:\boldsymbol{\Gamma}_{\boldsymbol{l}}^{\boldsymbol{B}_t}:\left(\boldsymbol{\delta b}_{\boldsymbol{t}}{}^{\boldsymbol{L}}:\dot{\boldsymbol{\varepsilon}}^{vp\boldsymbol{L}} - \boldsymbol{b}_{\boldsymbol{t}}{}^{\boldsymbol{L}}:\boldsymbol{A}^{\boldsymbol{B}_t}:\left(\boldsymbol{M}_{\boldsymbol{t}}^{\boldsymbol{e}}:\boldsymbol{\Sigma} + \dot{\boldsymbol{N}}^{\boldsymbol{e}} - \langle\dot{\boldsymbol{\varepsilon}}^{vp}\rangle\right)\right)\rangle \\
- \boldsymbol{Z}:\langle \boldsymbol{c}^{\boldsymbol{L}}:\boldsymbol{A}^{\boldsymbol{C}}:\left(\boldsymbol{\Gamma}_{\boldsymbol{l}}^{\boldsymbol{C}}:\boldsymbol{C}^{\boldsymbol{e}} - \boldsymbol{\Gamma}_{\boldsymbol{l}}^{\boldsymbol{B}_t}:\boldsymbol{B}_{\boldsymbol{t}}^{\boldsymbol{e}}\right):\left(\dot{\boldsymbol{\varepsilon}}^{vp\boldsymbol{L}} - \boldsymbol{A}^{\boldsymbol{B}_t}:\langle\dot{\boldsymbol{\varepsilon}}^{vp}\rangle\right)\rangle \\
+ \boldsymbol{Z}:\langle \boldsymbol{c}^{\boldsymbol{L}}:\boldsymbol{A}^{\boldsymbol{C}}:\left(\boldsymbol{\Gamma}_{\boldsymbol{l}}^{\boldsymbol{C}}:\boldsymbol{C}^{\boldsymbol{e}} - \boldsymbol{\Gamma}_{\boldsymbol{l}}^{\boldsymbol{B}_t}:\boldsymbol{B}_{\boldsymbol{t}}^{\boldsymbol{e}}\right):\left(\boldsymbol{A}^{\boldsymbol{B}_t}:\boldsymbol{\Gamma}_{\boldsymbol{l}}^{\boldsymbol{B}_t}:\left(\boldsymbol{b}_{\boldsymbol{t}}{}^{\boldsymbol{L}}:\dot{\boldsymbol{\eta}}^{\boldsymbol{L}} - \boldsymbol{B}_{\boldsymbol{t}}^{\boldsymbol{e}}:\dot{\boldsymbol{N}}^{\boldsymbol{e}}\right)\right)\rangle
\end{aligned}
\tag{11}
$$

with $\boldsymbol{Z} = \left(\boldsymbol{I} - \boldsymbol{S}^{\boldsymbol{e}}:\langle \boldsymbol{c}^{\boldsymbol{L}}:\boldsymbol{A}^{\boldsymbol{C}}:\boldsymbol{\Gamma}_{\boldsymbol{l}}^{\boldsymbol{C}}:\boldsymbol{c}^{\boldsymbol{L}}:\boldsymbol{A}^{\boldsymbol{C}}\rangle\right)^{-\boldsymbol{1}}:\boldsymbol{S}^{\boldsymbol{e}}$.

At the level of LS, we have $\dot{\boldsymbol{\varepsilon}}^{\boldsymbol{L}} = \boldsymbol{s}^{\boldsymbol{L}}:\dot{\boldsymbol{\sigma}}^{\boldsymbol{L}} + \dot{\boldsymbol{\varepsilon}}^{vp\boldsymbol{L}}$ with $\dot{\boldsymbol{\varepsilon}}^{vp\boldsymbol{L}} = \boldsymbol{m}_{\boldsymbol{t}}{}^{\boldsymbol{L}}:\boldsymbol{\sigma}^{\boldsymbol{L}} + \dot{\boldsymbol{\eta}}^{\boldsymbol{L}}$. $\boldsymbol{s}^{\boldsymbol{L}}$ (resp. $\mathbf{c}^{\boldsymbol{L}}$), $\boldsymbol{m}_{\boldsymbol{t}}{}^{\boldsymbol{L}}$ (resp. $\boldsymbol{b}_{\boldsymbol{t}}{}^{\boldsymbol{L}}$) and $\dot{\boldsymbol{\eta}}^{\boldsymbol{L}}$ are homogenized elastic compliances (resp. moduli), viscoplastic tangent compliances (resp. moduli) and viscoplastic back-extrapolated term for each LS. These tensors are now determined from the homogenization procedure at the mesoscale.

3.3. Mesoscale model: LS

3.3.1. Two-phase LS and averaging procedure

Here, we consider an infinite two-phase LS (see Figure 8). Both phases are ferrite (denoted "α") and austenite (denoted "γ") with volume fractions f^{α} and f^{γ}. For the present application, $f^{\alpha} = 0.25$, therefore $f^{\gamma} = 1 - f^{\alpha} = 0.75$. The volume averages of strain and stress tensors over each LS are given by:

$$\boldsymbol{\varepsilon}^{\boldsymbol{L}} = \langle\boldsymbol{\varepsilon}\rangle^{L} = f^{\gamma}\boldsymbol{\varepsilon}^{\boldsymbol{\gamma}} + f^{\alpha}\boldsymbol{\varepsilon}^{\boldsymbol{\alpha}} \tag{12a}$$

$$\boldsymbol{\sigma}^{\boldsymbol{L}} = \langle\boldsymbol{\sigma}\rangle^{L} = f^{\gamma}\boldsymbol{\sigma}^{\boldsymbol{\gamma}} + f^{\alpha}\boldsymbol{\sigma}^{\boldsymbol{\alpha}} \tag{12b}$$

where $\boldsymbol{\varepsilon}^{\boldsymbol{i}} = \boldsymbol{\varepsilon}^{\boldsymbol{e}\,\boldsymbol{i}} + \boldsymbol{\varepsilon}^{\boldsymbol{vp}\,\boldsymbol{i}} = \boldsymbol{s}^{\boldsymbol{i}} : \boldsymbol{\sigma}^{\boldsymbol{i}} + \boldsymbol{\varepsilon}^{\boldsymbol{vp}\,\boldsymbol{i}}$ with $\mathrm{i} = \alpha, \gamma$. The tensors $\boldsymbol{s}^{\boldsymbol{i}}$, $\boldsymbol{\varepsilon}^{\boldsymbol{i}}$, $\boldsymbol{\sigma}^{\boldsymbol{i}}$ and $\boldsymbol{\varepsilon}^{\boldsymbol{vp}\,\boldsymbol{i}}$ represent the elastic compliances, the strains, the Cauchy stresses and the viscoplastic strains of both phases at a given stress state during loading. Under the assumption of mean viscoplastic strain field in each phase, following strain compatibility and balance of linear momentum in the absence of body force, the strains and stresses are therefore piecewise uniform in the two-phase LS (see El Omri et al., 2000; Stupkiewicz and Petryk 2002; Franciosi and Berbenni, 2008; Berbenni et al. 2013; Richeton and Berbenni, 2013; Tiba et al., 2015; Richeton 2022).

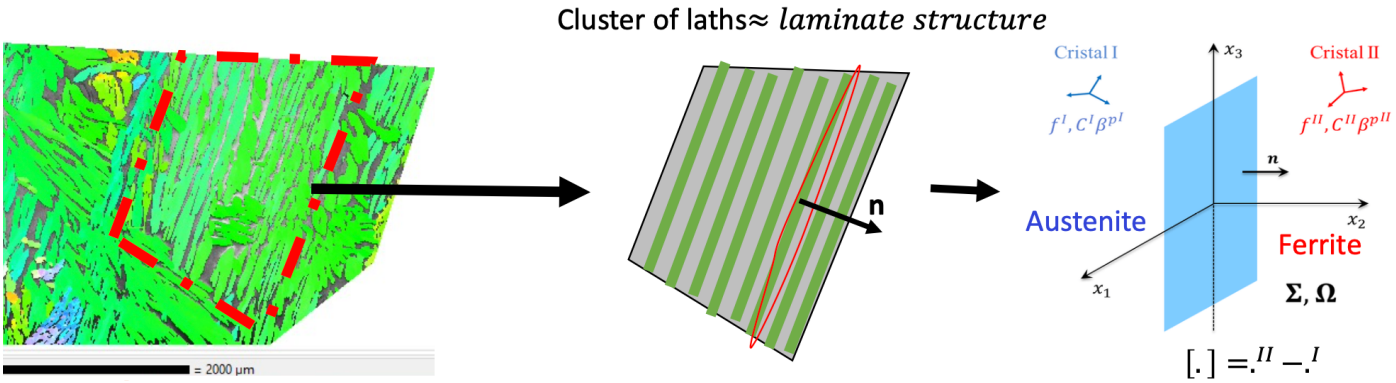

Figure 8: Schematic principle of the mesoscale model for the laminate structure (LS).

3.3.2. Strain/stress concentration equations for the laminate's model

The relationships between the strains and the stresses in each phase α and γ: $\boldsymbol{\varepsilon}^{\alpha,\gamma}, \boldsymbol{\sigma}^{\alpha,\gamma}$ and the strain and stress at the level of the LS; $\boldsymbol{\varepsilon}^{\boldsymbol{L}}, \boldsymbol{\sigma}^{\boldsymbol{L}}$ are calculated in the frame associated with the interface plane, i.e. the HP. Its unit outward normal **n** is supposed to be parallel to the $\mathbf{e_2}$ direction of a Cartesian frame ($\mathbf{e_1}$, $\mathbf{e_2}$, $\mathbf{e_3}$) and is directed from γ to α (see Figure 8).

In this frame, we adopt the following tensor to matrix convention (Nye, 1957) also known as the Voigt's notation, in which pairs of subscripts (ij) and (kl) are converted to single subscripts: (11)=1, (22)=2, (33)=3, (23) and (32)=4, (13) and (31)=5, (12) and (21)=6. In this notation, we will use indices i ranging from 1 to 6. The conventions for strains are the following: $\varepsilon_4 = 2\varepsilon_{23}, \varepsilon_5 = 2\varepsilon_{31}, \varepsilon_6 = 2\varepsilon_{12}$ and the components of the compliance matrix s_{ij} contain a multiplying factor of 2 if either i or j is equal to 4,5 or 6 and the other index is equal to 1, 2, 3, and, a multiplying factor of 4 if both i and j are equal to 4,5 or 6. Thus, each of the tensor components is associated with a matrix or a vector component. To determine the strain and stress concentration equations for the mesoscale model, the continuity conditions for stress and strain at the interface are invoked due to traction vector continuity and tangential strain continuity for perfectly bonded interface:

$$\varepsilon_P^{\alpha} = \varepsilon_P^{\gamma} = \varepsilon_P^{L} \qquad (13a)$$

$$\sigma_A^{\alpha} = \sigma_A^{\gamma} = \sigma_A^{L} \qquad (13b)$$

Where the in-plane components of strain and stress tensors are denoted *P = 1, 3, 5*, and the anti-plane ones are denoted *A = 2,4,6*, with the following constitutive laws using index notations:

$$\varepsilon_i^{\alpha,\gamma} = s_{ij}^{\alpha,\gamma}\sigma_j^{\alpha,\gamma} + \varepsilon_i^{vp\,\alpha,\gamma} \quad (i,j = 1,6) \qquad (14a)$$

$$\sigma_i^{\alpha,\gamma} = c_{ij}^{\alpha,\gamma}\left(\varepsilon_j^{\alpha,\gamma} - \varepsilon_j^{vp\,\alpha,\gamma}\right) = c_{ij}^{\alpha,\gamma}\varepsilon_j^{\alpha,\gamma} - \sigma_i^{vp\,\alpha,\gamma} \text{ with } \sigma_i^{vp\,\alpha,\gamma} = c_{ij}^{\alpha,\gamma}\varepsilon_j^{vp\,\alpha,\gamma} \quad (i,j = 1,6) \qquad (14b)$$

Starting from equations (14) and using equation (12a) together with equations (13), the strain concentration laws for both phases are given by:

$$\varepsilon_i^{\alpha} = \varepsilon_i^{L} - f^{\gamma} F_{ik}^{c}\left(\left[\!\left[c_{kj}\right]\!\right]\varepsilon_j^{L} - \left[\!\left[\sigma_k^{vp}\right]\!\right]\right) \quad (i,j,k = 1,6;\ \text{sum on } j,k) \tag{15a}$$

$$\varepsilon_i^{\gamma} = \varepsilon_i^{L} + f^{\alpha} F_{ik}^{c}\left(\left[\!\left[c_{kj}\right]\!\right]\varepsilon_j^{L} - \left[\!\left[\sigma_k^{vp}\right]\!\right]\right) \quad (i,j,k = 1,6;\ \text{sum on } j,k) \tag{15b}$$

where $[\![\cdot]\!] = (\cdot)^{\alpha} - (\cdot)^{\gamma}$ denotes the jump of fields or property, and, where the non-zero components of the symmetric matrix F_{ij}^{c} associated with c_{ij} is given analytically by:

$$F_{22}^{c} = (c_{44}^{*}c_{66}^{*} - c_{46}^{*2})/D \qquad F_{24}^{c} = (c_{26}^{*}c_{46}^{*} - c_{24}^{*}c_{66}^{*})/D \qquad F_{26}^{c} = (c_{24}^{*}c_{46}^{*} - c_{26}^{*}c_{44}^{*})/D$$

$$F_{44}^{c} = (c_{22}^{*}c_{66}^{*} - c_{15}^{*2})/D \qquad F_{46}^{c} = (c_{24}^{*}c_{26}^{*} - c_{22}^{*}c_{46}^{*})/D \qquad F_{66}^{s} = (c_{22}^{*}c_{44}^{*} - c_{24}^{*2})/D \tag{16}$$

with $D = c_{22}^{*}c_{44}^{*}c_{66}^{*} + 2c_{24}^{*}c_{46}^{*}c_{26}^{*} - c_{26}^{*2}c_{44}^{*} - c_{46}^{*2}c_{22}^{*} - c_{24}^{*2}c_{66}^{*}$ and $c_{ij}^{*} = f^{\gamma}c_{ij}^{\alpha} + f^{\alpha}c_{ij}^{\gamma}$.

Conversely, starting from equations (14) and using equation (12b) together with equations (13), the stress concentration laws for both phases are given by (see Richeton and Berbenni 2013; Tiba et al., 2015):

$$\sigma_i^{\alpha} = \sigma_i^{L} - f^{\gamma} G_{ik}^{s}\left(\left[\!\left[s_{kj}\right]\!\right]\sigma_j^{L} + \left[\!\left[\varepsilon_k^{vp}\right]\!\right]\right) \quad (i,j,k = 1,6;\ \text{sum on } j,k) \tag{17a}$$

$$\sigma_i^{\gamma} = \sigma_i^{L} + f^{\alpha} G_{ik}^{s}\left(\left[\!\left[s_{kj}\right]\!\right]\sigma_j^{L} + \left[\!\left[\varepsilon_k^{vp}\right]\!\right]\right) \quad (i,j,k = 1,6;\ \text{sum on } j,k) \tag{17b}$$

where the non-zero components of the symmetric matrix G_{ij}^{s} associated with s_{ij} are given analytically by:

$$G_{11}^{s} = (s_{33}^{*}s_{55}^{*} - s_{35}^{*2})/D \qquad G_{13}^{s} = (s_{15}^{*}s_{35}^{*} - s_{13}^{*}s_{55}^{*})/D \qquad G_{15}^{s} = (s_{13}^{*}s_{35}^{*} - s_{15}^{*}s_{33}^{*})/D$$

$$G_{33}^{s} = (s_{11}^{*}s_{55}^{*} - s_{15}^{*2})/D \qquad G_{35}^{s} = (s_{13}^{*}s_{15}^{*} - s_{11}^{*}s_{35}^{*})/D \qquad G_{55}^{s} = (s_{11}^{*}s_{33}^{*} - s_{13}^{*2})/D \tag{18}$$

with $D = s_{11}^{*}s_{33}^{*}s_{55}^{*} + 2s_{13}^{*}s_{35}^{*}s_{15}^{*} - s_{15}^{*2}s_{33}^{*} - s_{35}^{*2}s_{11}^{*} - s_{13}^{*2}s_{55}^{*}$ and $s_{ij}^{*} = f^{\gamma}s_{ij}^{\alpha} + f^{\alpha}s_{ij}^{\gamma}$.

3.3.3. Purely elastic homogenized behavior

Now, let us determine the effective elastic compliance $\boldsymbol{s^L}$ (resp. modulus $\mathbf{c^L}$) of each LS such that $\varepsilon_i^L = \mathrm{s}_{ij}^L \sigma_j^L$ or $\sigma_i^L = \mathrm{c}_{ij}^L \varepsilon_j^L$.

Using equation (12a) together with the linear elastic Hooke's law, we obtain:

$$\varepsilon_i^L = f^\gamma \mathrm{s}_{ij}^\gamma \sigma_j^\gamma + f^\alpha \mathrm{s}_{ij}^\alpha \sigma_j^\alpha = \mathrm{s}_{ij}^L \sigma_j^L \tag{19}$$

Then using both equations (17) with $\varepsilon_k^{vp} = 0$, together with equation (19), the homogenized elastic compliance for "L" reads (see Richeton and Berbenni 2013; Richeton 2022):

$$\mathrm{s}_{ij}^L = \langle \mathrm{s}_{ij} \rangle^L - f^\alpha f^\gamma [\![s_{ik}]\!] G_{kl}^s [\![s_{lj}]\!] \tag{20}$$

with $\langle \mathrm{s}_{ij} \rangle^L = f^\gamma \mathrm{s}_{ij}^\gamma + f^\alpha \mathrm{s}_{ij}^\alpha$.

Using equation (12b) together with the linear elastic Hooke's law, we obtain:

$$\sigma_i^L = f^\gamma \mathrm{c}_{ij}^\gamma \varepsilon_j^\gamma + f^\alpha \mathrm{c}_{ij}^\alpha \varepsilon_j^\alpha = \mathrm{c}_{ij}^L \varepsilon_j^L \tag{21}$$

Then, using both equations (15) with $\sigma_k^{vp} = 0$, together with equation (21), the homogenized elastic stiffness for "L" reads:

$$\mathrm{c}_{ij}^L = f^\gamma \mathrm{c}_{ij}^\gamma + f^\alpha \mathrm{c}_{ij}^\alpha - f^\alpha f^\gamma [\![c_{ik}]\!] F_{kl}^c [\![c_{lj}]\!] \tag{22}$$

3.3.4. Purely affine viscoplastic homogenized behavior

For purely affine viscoplastic two-phase LS, we consider the following thermo-elastic like linear comparison material for both phases α and γ:

$$\dot{\varepsilon}_i^{\alpha,\gamma} = \dot{\varepsilon}_i^{vp\,\alpha,\gamma} = m_{t\,ij}^{\alpha,\gamma} \sigma_j^{\alpha,\gamma} + \dot{\eta}_i^{\alpha,\gamma} \quad (i,j = 1,6) \tag{23a}$$

$$\sigma_i^{\alpha,\gamma} = b_{t\,ij}^{\alpha,\gamma} \left(\dot{\varepsilon}_j^{\alpha,\gamma} - \dot{\eta}_j^{\alpha,\gamma} \right) = b_{t\,ij}^{\alpha,\gamma} \dot{\varepsilon}_j^{\alpha,\gamma} - b_{t\,ij}^{\alpha,\gamma} \dot{\eta}_j^{\alpha,\gamma} \qquad (i,j = 1,6) \tag{23b}$$

with the following continuity conditions for the purely viscoplastic problem:

$$\dot{\varepsilon}_P^\alpha (= \dot{\varepsilon}_P^{vp\,\alpha}) = \dot{\varepsilon}_P^\gamma (= \dot{\varepsilon}_P^{vp\,\gamma}) = \dot{\varepsilon}_P^L \left(= \dot{\varepsilon}_i^{vp\,L} \right) \tag{24a}$$

$$\sigma_A^\alpha = \sigma_A^\gamma = \sigma_A^L \tag{24b}$$

and the volume averages on the laminate:

$$\dot{\varepsilon}_i^L = \langle \dot{\varepsilon}_i \rangle^L = f^\gamma \dot{\varepsilon}_i^\gamma + f^\alpha \dot{\varepsilon}_i^\alpha \tag{25a}$$

$$\sigma_i^L = \langle \sigma_i \rangle^L = f^\gamma \sigma_i^\gamma + f^\alpha \sigma_i^\alpha \tag{25b}$$

For this purely viscoplastic problem, similar strain concentration equations are found by substituting in equation (15) $\dot{\varepsilon}_i^\alpha, \dot{\varepsilon}_i^\gamma, \dot{\varepsilon}_j^L, F_{ik}^{b_t}, b_{t_{kj}}, b_{t_{kj}} \dot{\eta}_j$ for $\varepsilon_i^\alpha, \varepsilon_i^\gamma, \varepsilon_j^L, F_{ik}^c, c_{kj}, \sigma_k^{vp}$, respectively:

$$\dot{\varepsilon}_i^{\alpha} = \dot{\varepsilon}_i^{L} - f^{\gamma} F_{ik}^{b_t} \left(\left[\!\left[b_{t_{kj}} \right]\!\right] \dot{\varepsilon}_j^{L} - \left[\!\left[b_{t_{kj}} \dot{\eta}_j \right]\!\right] \right) \quad (i,j,k = 1{,}6;\ \text{sum on } j,k) \tag{26a}$$

$$\dot{\varepsilon}_i^{\gamma} = \dot{\varepsilon}_i^{L} + f^{\alpha} F_{ik}^{b_t} \left(\left[\!\left[b_{t_{kj}} \right]\!\right] \dot{\varepsilon}_j^{L} - \left[\!\left[b_{t_{kj}} \dot{\eta}_j \right]\!\right] \right) \ (i,j,k = 1{,}6;\ \text{sum on } j,k) \tag{26b}$$

where the non-zero components of the symmetric matrix $F_{ij}^{b_t}$ associated with $b_{t_{ij}}$ are given by substituting $b_{t_{ij}}$ for c_{ij} in equation (16). Using equation (23b) together with equation (25b) yields:

$$\sigma_i^{L} = f^{\gamma} \left(b_{t\,ij}^{\gamma}\, \dot{\varepsilon}_j^{\gamma} - b_{t\,ij}^{\gamma}\, \dot{\eta}_j^{\gamma} \right) + f^{\alpha} \left(b_{t\,ij}^{\alpha}\, \dot{\varepsilon}_j^{\alpha} - b_{t\,ij}^{\alpha}\, \dot{\eta}_j^{\alpha} \right) = b_{t\,ij}^{L}\, \dot{\varepsilon}_j^{L} + \zeta_i^{L} \tag{27}$$

with the back-extrapolated stress $\zeta_i^{L} = -b_{t\,ij}^{L}\, \dot{\eta}_j^{L}$. Introducing both equations (26) in equation (27) yields:

$$b_{t\,ij}^{L} = \langle b_{t\,ij} \rangle^{L} - f^{\alpha} f^{\gamma} [\![b_{t\,ik}]\!] F_{kl}^{b_t} [\![b_{t\,lj}]\!] \tag{28}$$

with $\langle b_{t\,ij} \rangle^{L} = f^{\gamma} b_{t\,ij}^{\gamma} + f^{\alpha} b_{t\,ij}^{\alpha}$, and:

$$\zeta_i^{L} = \langle \zeta_i \rangle^{L} + f^{\alpha} f^{\gamma} [\![b_{t\,ik}]\!] F_{kl}^{b_t} [\![\zeta_l]\!] \tag{29}$$

with $\langle \zeta_i \rangle^{L} = f^{\gamma} \zeta_i^{\gamma} + f^{\alpha} \zeta_i^{\alpha}$.

Conversely, similar stress concentration equations are found by substituting in equation (17): $G_{ik}^{m_t}$, $m_{t_{kj}}, \dot{\eta}_k$ for $G_{ik}^{s}, s_{kj}, \varepsilon_k^{vp}$, respectively:

$$\sigma_i^{\alpha} = \sigma_i^{L} - f^{\gamma} G_{ik}^{m_t} \left(\left[\!\left[m_{t_{kj}} \right]\!\right] \sigma_j^{L} + [\![\dot{\eta}_k]\!] \right) \quad (i,j,k = 1{,}6;\ \text{sum on } j,k) \tag{30a}$$

$$\sigma_i^{\gamma} = \sigma_i^{L} + f^{\alpha} G_{ik}^{m_t} \left(\left[\!\left[m_{t_{kj}} \right]\!\right] \sigma_j^{L} + [\![\dot{\eta}_k]\!] \right) \ (i,j,k = 1{,}6;\ \text{sum on } j,k) \tag{30b}$$

where the non-zero components of the symmetric matrix $G_{ij}^{m_t}$ associated with $m_{t_{ij}}$ are given by substituting $m_{t_{ij}}$ for s_{ij} in equation (18). Using equation (23a) together with equation (25a) yields

$$\dot{\varepsilon}_i^{L} = f^{\gamma} \left(m_{t\,ij}^{\gamma} \sigma_j^{\gamma} + \dot{\eta}_i^{\gamma} \right) + f^{\alpha} \left(m_{t\,ij}^{\alpha} \sigma_j^{\alpha} + \dot{\eta}_i^{\alpha} \right) = m_{t\,ij}^{L} \sigma_j^{L} + \dot{\eta}_i^{L} \tag{31}$$

Then, using equations (30) in equation (31) yields:

$$m_{t\,ij}^{L} = \langle m_{t\,ij} \rangle^{L} - f^{\alpha} f^{\gamma} [\![m_{t\,ik}]\!] G_{kl}^{\mathrm{m_t}} [\![m_{t\,lj}]\!] \tag{32}$$

with $\langle m_{t\,ij} \rangle^{L} = f^{\gamma} m_{t\,ij}^{\gamma} + f^{\alpha} m_{t\,ij}^{\alpha}$, and:

$$\dot{\eta}_i^{L} = \langle \dot{\eta}_i \rangle^{L} - f^{\alpha} f^{\gamma} [\![m_{t\,ik}]\!] G_{kl}^{\mathrm{m_t}} [\![\dot{\eta}_l]\!] \tag{33}$$

with $\langle \dot{\eta}_i \rangle^L = f^\gamma \dot{\eta}_i^\gamma + f^\alpha \dot{\eta}_i^\alpha$.

It is noteworthy that equations (20) and (22) and equations (28) and (32) are consistent from the homogenization theory (see e.g. Qu and Cherkaoui, 2006), since $\mathbf{s}^L = \mathbf{c}^{L^{-1}}$, $\boldsymbol{m_t}^L = \boldsymbol{b_t}^{L^{-1}}$.

Furthermore, it can be seen from these expressions that the method is not limited to elastic and viscoplastic Reuss (iso-stress) or Voigt (iso-strain, i.e. Taylor,1938) assumptions, which are crude assumptions usually used to model duplex steels in the literature (Verhaeghe, 1996; M'Cirdi, 2000).

3.4. Microscale model: single crystal

The local elastoviscoplastic behavior is described within a crystal plasticity framework. The constitutive equations developed by Méric and Cailletaud (1991a,b) are used to model the behavior of crystalline laths in both the f.c.c. structure for austenitic laths and in the b.c.c. structure for ferritic laths. This model, which is of phenomenological nature, depends on a limited number of materials parameters, which is better candidate for expected structural calculations expected with the present multiscale model. The viscoplastic strain rate is given by crystal plasticity in both phases:

$$\dot{\boldsymbol{\varepsilon}}^{\boldsymbol{vp}} = \sum_{s=1}^{N} \boldsymbol{R}^{\boldsymbol{s}} \dot{\gamma}^s \tag{34}$$

Equation (34) describes the sum of the contributions of all active slip systems (i.e. $\dot{\gamma}^s \neq 0$) in each single crystalline phase. The driving force for slip is given by the resolved shear stress τ^s, defined as:

$$\tau^s = \boldsymbol{R}^s : \boldsymbol{\sigma} \tag{35}$$

with $\boldsymbol{R^s}$ the symmetric Schmid orientation tensor:

$$R_{ij}^s = \frac{1}{2}\left(n_i^s l_j^s + n_j^s l_i^s\right) \tag{36}$$

where n_i^s and l_i^s are unit vectors normal to slip plane and parallel to slip directions.

The behavior of the single crystal (cubic crystals for both phases) is supposed to be elastic-viscoplastic for both phases at small strains, where plastic distortion results from crystallographic slips on specific systems s defined by a plane normal n^s and a slip direction l^s. Here, the effect of lattice rotation evolution is neglected as in previous studies on the same material (see Bugat et al.,1999; Bugat, 2000). For f.c.c. crystals (austenite), 12 octahedral slip systems of type (111) <110>. Following previous studies in duplex steels (Bugat et al., 1999; Bugat 2000; Verhaeghe et al. 1996, 1997), we assume that only the dense systems (110) <111> are activated in the ferrite (b.c.c). This assumption is made due to the KS-OR, which favors such family of slip systems in the b.c.c. structure.

The phenomenological model with hardening variables developed by Méric and Cailletaud (1991a,b) is used to describe the viscoplastic slip rate $\dot{\gamma}^s$:

$$\dot{\gamma}^s = \left\langle \frac{|\tau^s - x^s| - r^s}{K} \right\rangle^n sign(\tau^s - x^s) \tag{37}$$

where $\langle x \rangle = max(x, 0)$. In equation (37), x^s and r^s are the kinematic and the isotropic hardening shear stresses, respectively, given by their rates:

$$\dot{x}^s = c \quad \dot{\gamma}^s - d \quad x^s |\dot{\gamma}^s| \tag{38}$$

and:

$$\dot{r}^s = \sum_{r=1}^{N} bQH_{sr} \exp(-b \quad v^r) |\dot{\gamma}^r| \tag{39}$$

where $v^r = \int |\dot{\gamma}^r| \, dt$.

In the above equations, K and n are two material coefficients characterizing the viscous effect, c, b, d and Q are hardening parameters, H_{sr} is an $\mathrm{N} \times \mathrm{N}$ matrix describing the interactions between the different slip systems, where N is the total number of the slip systems in both austenite and ferrite single crystals (here $\mathrm{N} = 12$ for both the f.c.c. and b.c.c. slip systems). Therefore, at the grain level, the viscoplastic strain rate is given by:

$$\dot{\boldsymbol{\varepsilon}}^{\boldsymbol{vp}} = \sum_{s=1}^{N} \boldsymbol{R^s} \left\langle \frac{|\tau^s - x^s| - r^s}{K} \right\rangle^n sign(\tau^s - x^s) \tag{40}$$

According to the "affine" formulation used in this study (see Equation (2)), the tangent viscoplastic compliance tensor $\mathbf{m_t} = \partial \dot{\boldsymbol{\varepsilon}}^{\mathbf{vp}} / \partial \boldsymbol{\sigma}$ and $\dot{\boldsymbol{\eta}}$ write in index notation, as:

$$m_{t,ijkl} = \sum_{s=1}^{N} \frac{n}{K} \left\langle \frac{|\tau^s - x^s| - r^s}{K} \right\rangle^{n-1} R_{ij}^s R_{kl}^s \tag{41}$$

and:

$$\dot{\eta}_{ij} = \sum_{s=1}^{N} R_{ij}^s \left\langle \frac{|\tau^s - x^s| - r^s}{K} \right\rangle^n sign(\tau^s - x^s) - \sum_{s=1}^{N} \frac{n}{K} \left\langle \frac{|\tau^s - x^s| - r^s}{K} \right\rangle^{n-1} R_{ij}^s \tau^s \tag{42}$$

Then, equations (41) and (42) are used at the level of the mesoscale model (LS) in equations (32) and (33), or, in equations (28) and (29).

4. Simulation results

4.1. Crystal plasticity parameters

First, the crystal plasticity parameters were identified on the tensile curve for the non-aged material subjected to a strain rate of $\dot{E} = 2 \times 10^{-4} s^{-1}$ in the X-direction (Figure 9(a)). The material's response is predicted with the poly-bicrystal's model, i.e. at macroscale 2. The elastic properties of the material are supposed to be isotropic with $E = 200$ GPa (Young's modulus) and $\nu = 0.3$ (Poisson ratio). For the poly-bicrystal's model, the Representative Volume Element (RVE) is considered as an aggregate of 15 ferritic grains with volume fractions following the fractions of these grains obtained from EBSD measurements, see Figure 1 and Table A.1 for their crystallographic orientations with respect to the Cartesian frame (X, Y, Z). Then, each ferritic grain contains 24 laminate structures (LS) in spherical domains with equal volume fractions $f^L = 1/24$. It is then assumed that the occurrence probability of each variant is equal with no specific variant selection. This assumption follows the EBSD analysis, which does not display the predominance of specific variants. The identified Méric and Cailletaud (1991a,b)'s crystal plasticity parameters are reported in Table 3. Let us note that the intra-granular kinematic hardening parameters, i.e. the constants *c* and *d* in equation (30), were set to zero since no experimental cyclic curves were used to identify these parameters.

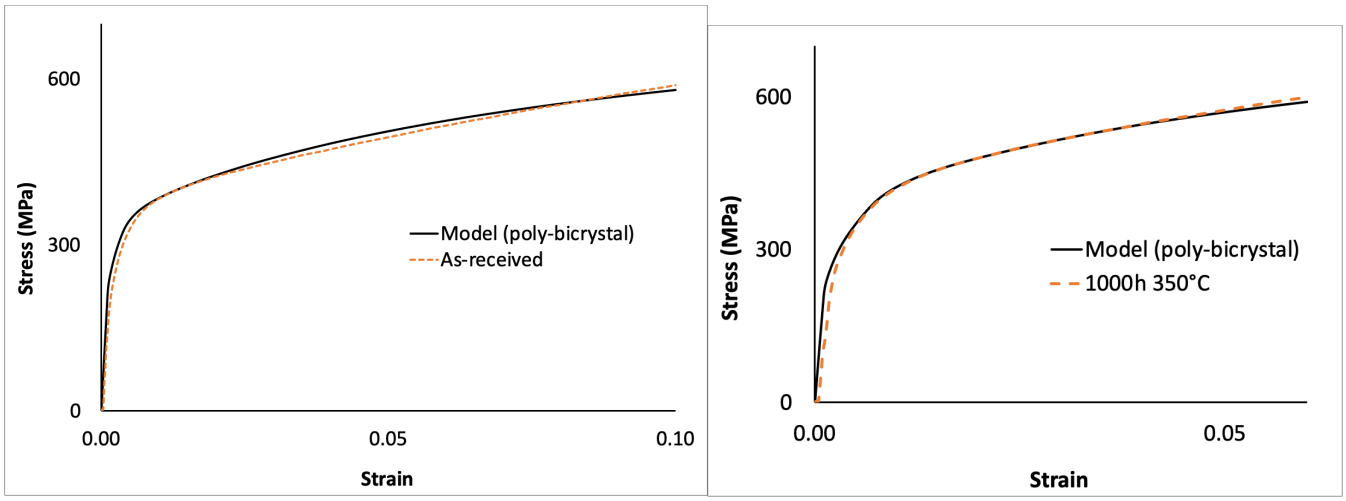

(a) (b)

Figure 9: Identification of crystal plasticity parameters for both phases using the tensile curves of the as-received specimen (a); and the aged specimen (b).

Table 3. Viscoplastic flow rule and hardening parameters (Méric-Cailletaud's law) for both phases identified on the non-aged and aged experimental tensile curves.

	n	$K(MPa.s^{1/n})$	$r_0(MPa)$	b	q	c	d	H_{sr}
Austenite FCC {111} <110> 12 slip systems	10	20	95	13	36	0	0	1
Non-aged Ferrite BCC {110} <111> 12 slip systems	10	20	260	20	95	0	0	1
Aged Ferrite: BCC {110} <111> 12 slip systems	10	20	400	25	105	0	0	1

4.2. Numerical assessment for one KS-OR variant with full-field EVPFFT at mesoscale

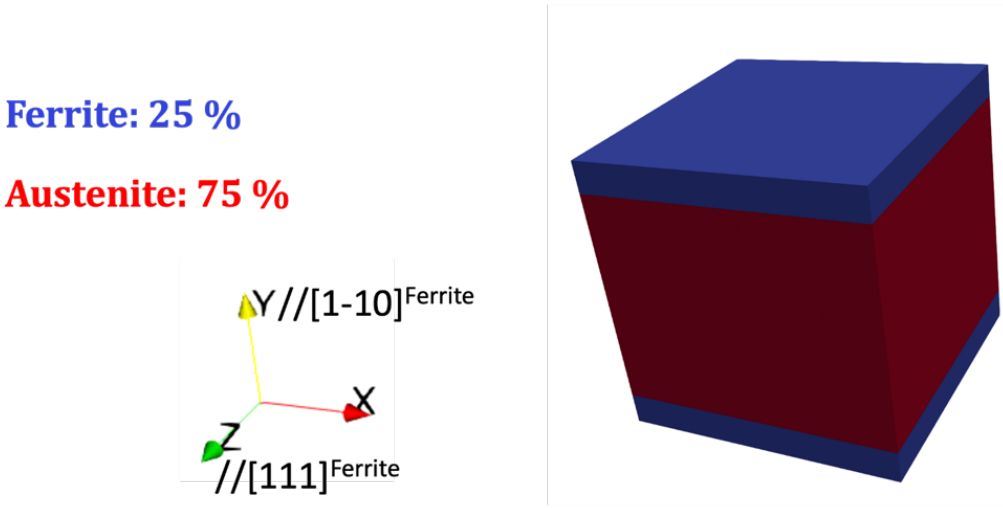

Figure 10: Two-phase laminate configuration for the first KS-OR in the list of Table 2. The calculations are made with the mean field mesoscale model for one laminate structure (LS). Numerical comparisons with unit cell calculations using the EVPFFT model.

In a first part, it is important to discuss and validate the micromechanical model chosen at the mesoscale in Figure 5". One KS-OR variant is chosen, i.e. the first variant among the list of the 24 variants denoted V1 in Table 2. In the simulation, the Cartesian coordinate system (X, Y, Z) is fixed with the HP, i.e. the interface between both phases, with unit normal **n** parallel to the Y-axis (// $[1\ \bar{1}0]\alpha$), while the X-axis and the Z-axis (// $[1\ 1\ 1]\alpha$) are parallel to the habit plane (see Figure 10).

The volume fraction of ferrite (blue colored phase in Figure 10) is set to 25% to be consistent with the experimental data and the Euler-Bunge angles for ferrite in this configuration is given by: $\phi_1 = 90°, \phi = 54.74°, \phi_2 = 45°$. The volume fraction of austenite (red colored phase on Figure 10) is set to 75% with Euler-Bunge angles: $\phi_1 = 125.27°, \phi = 90°, \phi_2 = 45°$.

The monotonic tensile responses simulated with the mean field model along the X-, Y-, Z-directions with applied strain rate $\dot{E} = 10^{-3}s^{-1}$ are first compared to full-field calculations performed with the EVPFFT formulation (elastoviscoplastic FFT). In Figure 11, the average stresses vs. average strains over the LS (black colored curves), ferrite (blue colored curve) and austenite (red colored curve) are reported. Here, the EVPFFT formulation, first developed by Lebensohn et al. (2012), was adapted with the numerical implementation of the Méric and Cailletaud (1990a,b)'s crystal plasticity laws reported in section 3.4 (see dotted curves). It is checked that for the three directions, a very good match is obtained showing the relevance of the present mean field model at the mesoscale, which does not need full field calculations and is less computational. Therefore, the analytic formulae introduced in section 3.3. are validated against full field calculations.

The largest stress differences between both phases and between the overall behavior of the laminate composite are obtained for the Z- and the X- tensile loading directions, i.e. parallel to the HP. Then, large incompatibility stresses are observed for these tensile directions, while uniform strain is present. In contrast, due to traction continuity at the HP, the same stress is obtained in both phases for the case where the tensile direction is parallel to the Y-direction, but the strains are not uniform anymore. Let us note that other parameters can be used with intra-granular kinematical hardening in austenite, and the mean field model was also validated against full field FFT simulations using the EVPFFT model with Méric-Cailletaud's crystal plasticity laws during cyclic loadings (see Tsekpuia, 2022).

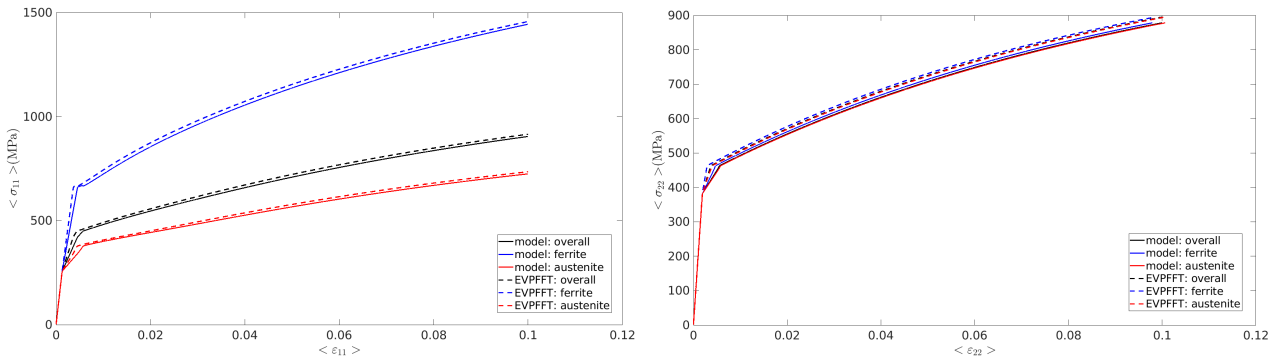

(a) (b)

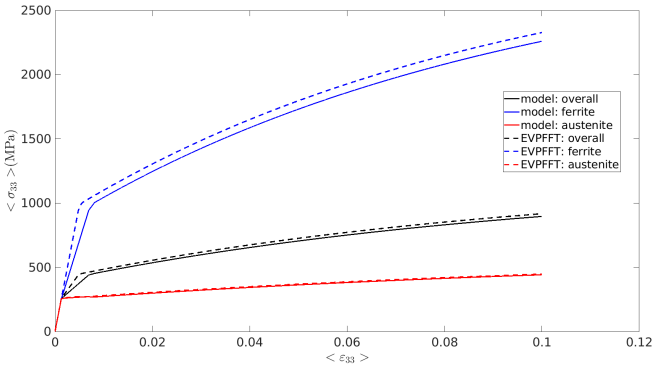

(c)

Figure 11: Monotonic tensile responses simulated with the mean field model at meso-scale (solid lines) along the: (a) X-, (b) Y-, (c) Z-directions with applied stain rate $\dot{E} = 10^{-3}s^{-1}$ compared to full-field EVPFFT calculations with periodic boundary conditions and same applied strain rate (dotted lines). The reported stresses are the average stresses in ferrite, austenite and in the laminate (overall).

The responses of the mean field model are now compared with the individual single crystalline responses which are simulated separately for same boundary conditions (see the curves with dotted lines in Figure 12). The objective is to study the influence of the strain-hardening behavior of each phase compared to the role of incompatibility stresses on the stress/strain responses and on slip activity. Regarding the X-direction, a larger hardening rate is observed in the case of the LS in both phases (solid lines) compared to single crystalline responses (dotted lines) due to internal stresses in both phases, see Figure 12(a). The active slip systems are B4, C1 for single austenite and 2A, 4D for single ferrite (see Table A.3 and A.4 in the Appendix for notations), which correspond to a double slip configuration in both crystals and follows the classic Schmid factor analysis. When the LS is considered with the KS OR (V1), slip activity changes from double to multiple slip and new slip systems are activated with additional slip systems B5, A3, C5, A2, for austenite, and 6A, 6D, 1C, 3C, for ferrite. In the Y-direction, single crystal hardening curves exhibit a difference of about 500 MPa at 10% of strain, where ferrite (b.c.c.) is harder than austenite (f.c.c.), see Figure 12(b). In contrast, the LS leads to equal stress in both phases, which corresponds to the volume average of the individual single crystalline stresses (composite effect on the stress only). For single crystals, slip activity is governed by 4 slip systems for ferrite (2A, 3A, 1D, 4D) and 6 ones for austenite (B2, C3, B5, C5, A2, A3). It is noteworthy that the same active slip systems are present in the LS, due to the isostress condition. The uniaxial tension in the Z-direction (i.e. // $[1\,1\,1]\alpha$) displays similar behavior between single crystal responses and phase responses in the laminate. In this case, there is a negligible composite effect, so that the hardening behavior in both phases of the laminate is mainly dictated by the single crystalline behaviors. The slip analysis shows similar trends between

single crystalline and bi-crystalline responses with the activations of B2, B4, C1, C3 for austenite and 3C, 1C, 6D, 6A, 1D, 3A for ferrite.

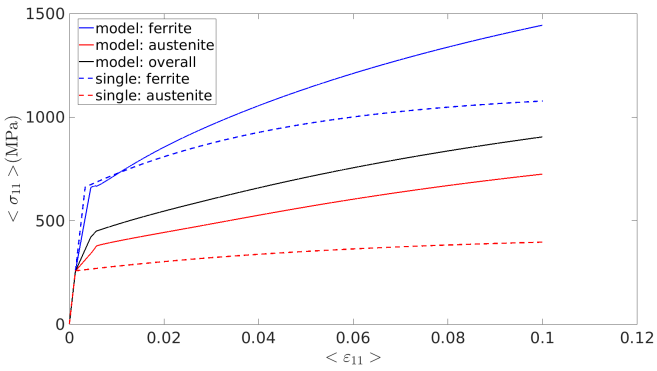

(a)

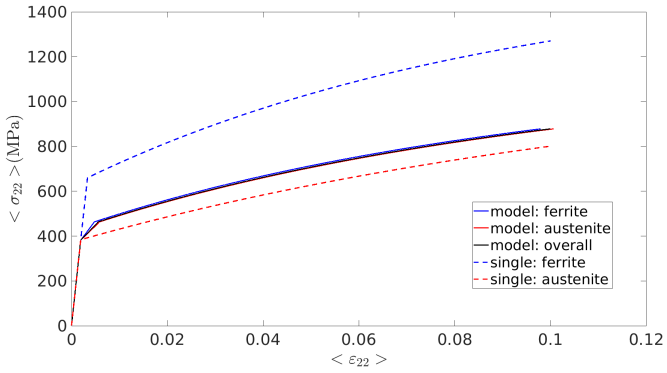

(b)

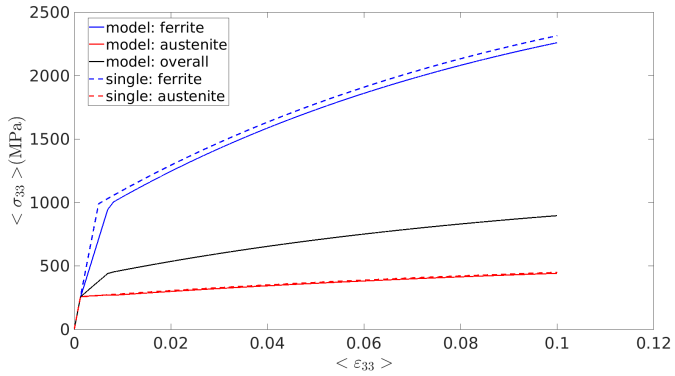

(c)

Figure 12: Monotonic tensile responses simulated with the mean field model at meso-scale (solid lines) along the: (a) x-, (b) y-, (c) z-directions with applied stain rate $\dot{E} = 10^{-3}s^{-1}$ compared to single crystalline responses with same boundary conditions (dotted lines). The reported stresses are the average stresses in ferrite, austenite and in the laminate (overall).

4.3. Bicrystal responses for an aggregate of 24 KS-OR variants due to the tensile loading along the [100]-direction in ferrite

Let us consider a first case where the calculations are performed in the Cartesian frame related to ferrite. Hence, the crystallographic orientation of ferrite is supposed to be given by the Euler-Bunge angles: $\phi_1 = 0°, \phi = 0°, \phi_2 = 0°$. In this case, the Euler-Bunge angles for the 24 KS-OR variants are given in Table 2. The Representative Volume Element (RVE) considered for the bicrystal forming one primary ferritic grain and defining the macroscale 1 (see Figure 5) is constituted of 24 LS (see Figures 6 and 7). It is subjected to a tensile loading along the X-axis with applied strain rate $\dot{E} = 10^{-3}s^{-1}$.

Figure 13 shows the distribution of normal stresses along the tensile direction in ferrite (σ_{11}) corresponding to the stresses parallel to $[100]\alpha$, as a function of applied tensile strain (E_{11}). These calculations are useful to determine the stresses normal to a cleavage plane in ferrite (α) which are {100} α -type plane (see Bugat et al. 1999, 2001; Bugat, 2000, M'Cirdi, 2000; M'Cirdi et al., 2001). Three groups of variants with different mechanical behaviors can be clearly identified: two groups exhibit stresses reaching a range between 500-600 MPa at 10% of tensile strain, and one group reflects higher stresses exceeding 1000 MPa at 10% of tensile strain.

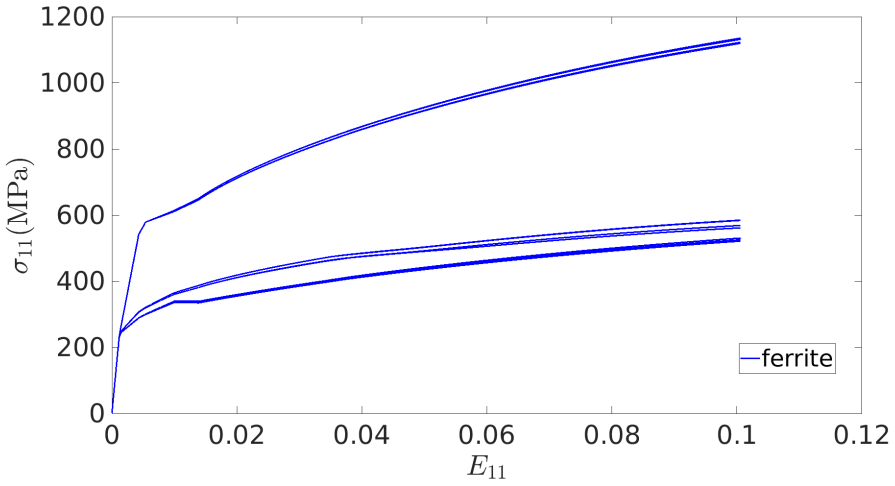

Figure 13: Stresses in ferrite as a function of macroscopic tensile strain (in the X-direction or along $[100]\alpha$) for the 24 KS-OR variants.

The analysis of these three groups in terms of local strains/stresses in both phases is reported. The first group corresponds to variants V1, V3, V5, V7, V13, V15, V21, V23 with only Bain group B1 (see Figure 14). The second one corresponds to variants V2, V4, V6, V8, V14, V16, V22, V24 (see Figure 15), and the third one corresponds to variants V9, V10, V11, V12, V17, V18, V19, V20 (see Figure 16). We notice that each of the three groups contains specific HP. According to Table 2, it is seen that the first two groups with lower stresses (Figures 14 and 15) contain HP: H1, H2, H3, H4, whereas the third group, which give higher stresses (Figure 16) is only constituted of HP: H5 and H6. Therefore, it is shown that the HP parallel to the loading direction (X-axis) like H5 and H6 give to highest strains and stresses in ferrite associated with these variants. The stresses in ferrite and austenite for these variants are much different from the averaged stress at the mesoscale for each variant (green colored solid lines) and the macroscopic average stress at the scale of the primary ferritic grain (black colored solid lines). The strains in both phases are uniform. This mechanical behavior looks like the single LS responses in Figures 11(a) and 11(c). In the case of HP: H1 to H4, they are oriented at 45° with respect to the X-tensile loading axis. For each variant with H1 to H4,

stress difference is not observed but a large strain discrepancy is present between both phases and the mesoscale and macroscopic average responses (see Figures 14 and 15).

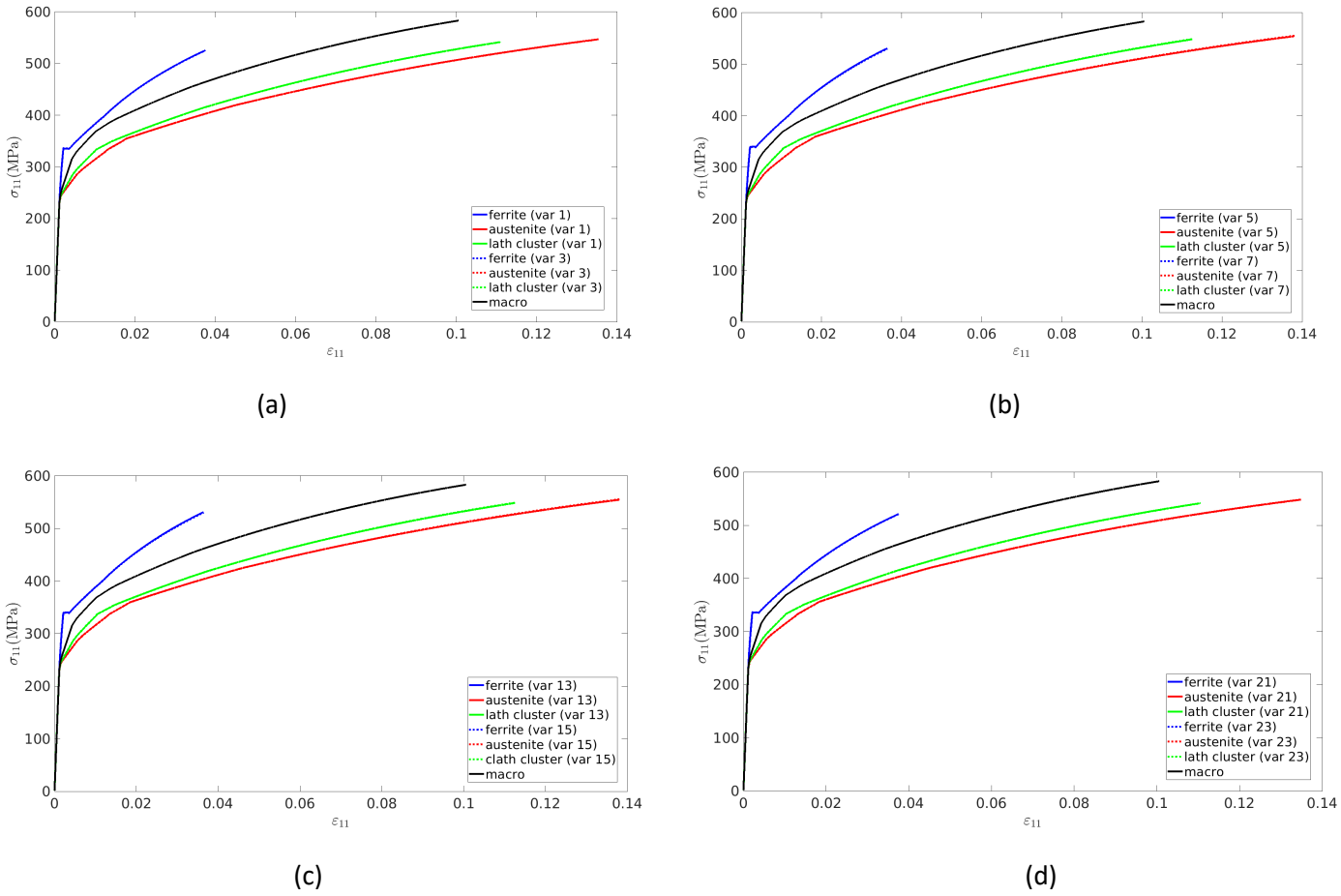

Figure 14: Stress/strain responses according to the x-direction for the *first group of variants* : (a) 1, 3 (H1, B1); (b) 5, 7 (H3, B1); (c) 13, 15 (H4, B1); (d) 21, 23 (H2,B1)

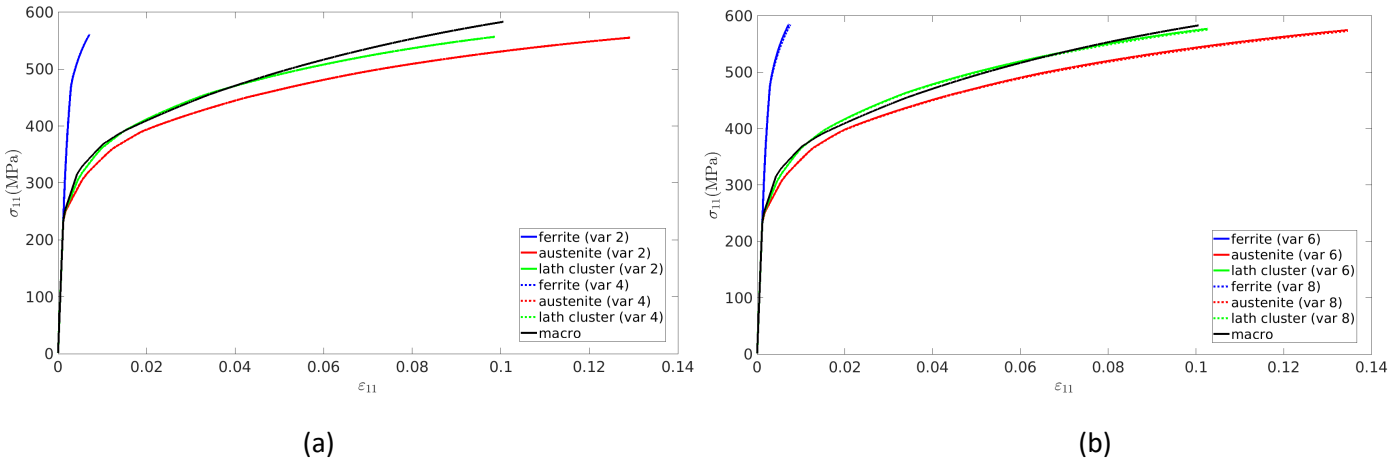

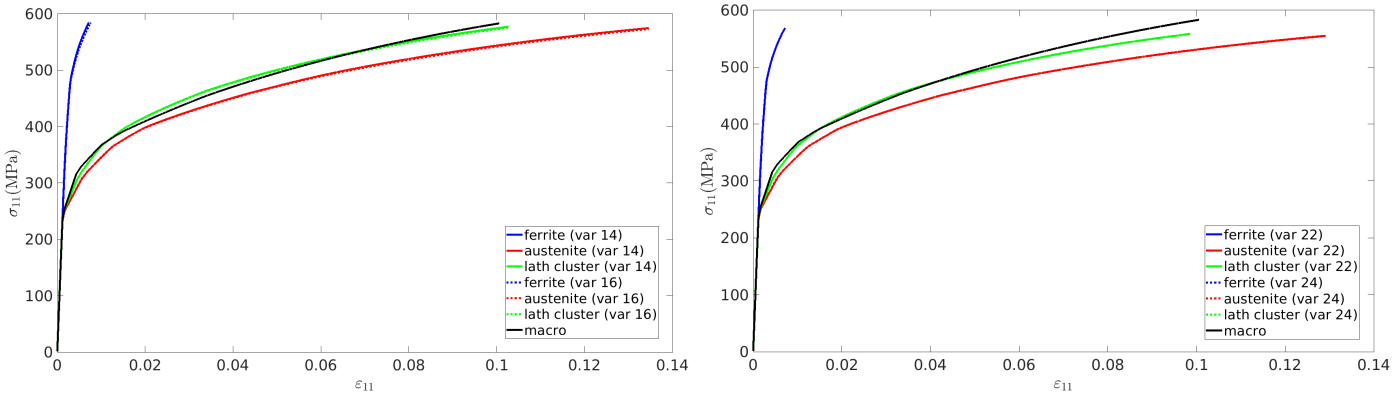

(c) (d)

Figure 15: Stress/strain responses according to x-direction for the *second group of variants*: (a) 2, 4 (H2, B2); (b) 6, 8 (H4, B3); (c) 14, 16 (H3, B3); (d) 22, 24 (H1,B2)

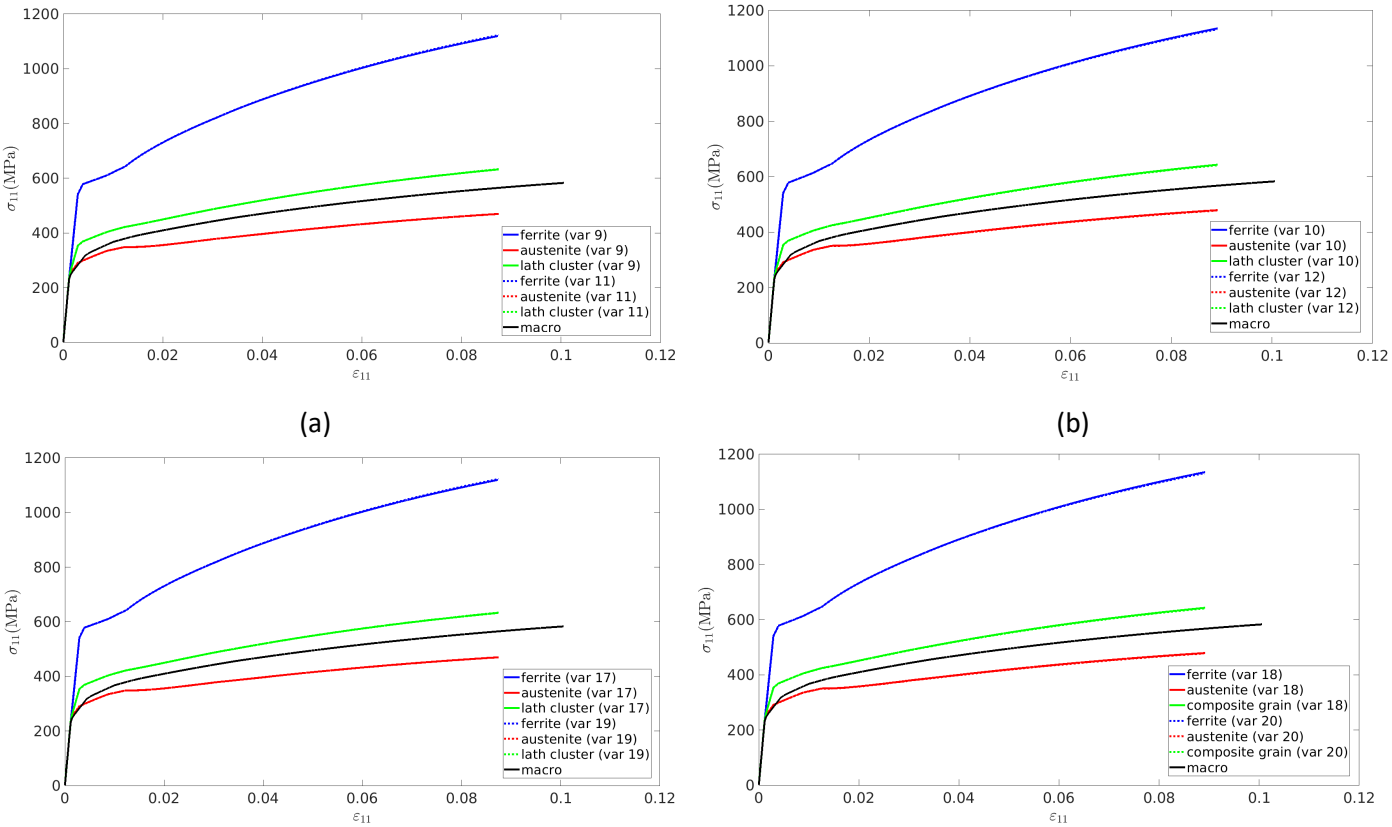

(a) (b)

(c) (d)

Figure 16: Stress/strain responses according to x-direction for the *third group of variants*: (a) 9, 11 (H5, B2); (b) 10, 12 (H6, B3); (c) 17, 19 (H6, B2); (d) 18, 20 (H5, B6).

4.4. Bicrystal responses: effect of primary ferritic grain crystallographic orientation

In this section, the role of primary ferritic grain orientation is investigated. Then, we consider here the crystallographic orientation of the first ferritic grain in the list: $\phi_1 = 18.11°, \phi = 40.12°, \phi_2 = 7.52°$ (see Table A.1 in Appendix). It corresponds to the largest grain of the specimen (green colored on the left part of Figure 4). Figure 17 shows the stress heterogeneities in ferrite among variants for

this orientation (here the stress component along the X-direction). Overall, these stress heterogeneities are more important than for the initial orientation $\phi_1 = 0°, \phi = 0°, \phi_2 = 0°$, see Figure 13. The clear separation into three well defined groups of variants as in Figure 13 vanishes. For each previous group, there is now a large scatter of stress responses in ferrite due to primary ferritic grain orientation which breaks the symmetries of the HP in the KS-OR variants with respect to the loading axis. Figure 18 shows the axial stresses for austenite, ferrite and the averaged responses at the mesoscale and at the macro-scale 1 for the first group (V1, V3, V5, V7, V13, V15, V21, V23). It is shown that the highest stresses in ferrite are found for variants V5, V7, V21, V23. Figure 19 shows the axial stresses for austenite, ferrite and the averaged responses at the mesoscale and at the macroscale 1 for the second group (V2, V4, V6, V8, V14, V16, V22, V24). It is shown that the stresses in ferrite are lower than the ones in the first group: the highest stresses are found with V2, V14, V16. In these groups, the variants V6, V8, V13, V15 still exhibit very low strains in ferrite compared to austenite as in the case of the initial orientation (see Figures 14(b) and 15(b)). In the third group (V9, V10, V11, V12, V17, V18, V19, V20), the stresses in ferrite remain high (around 1000 MPa at 10% of strain) and the strains are more uniform, which corroborates the results found in Figure 16. However, there are now small discrepancies between the different variants of this group due to the crystallographic orientation of the ferritic grain.

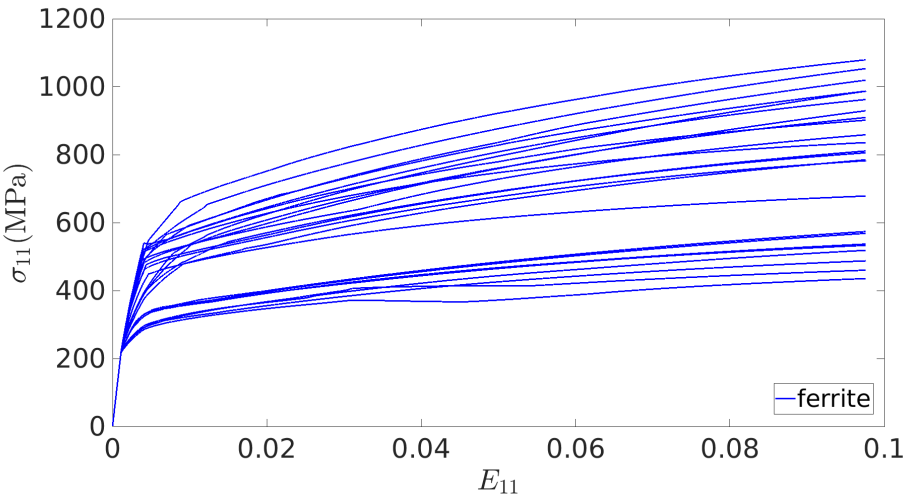

Figure 17: Stresses in ferrite for the 24 different KS-OR variants as a function of macroscopic strain according to the X-direction for the ferrite orientation: $\phi_1 = 18.11°, \phi = 40.12°, \phi_2 = 7.52°$.

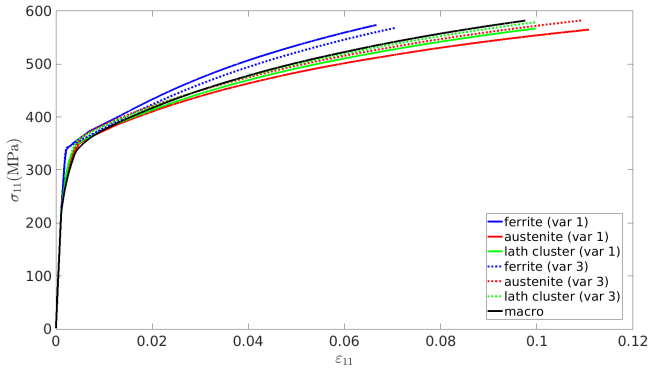

(a)

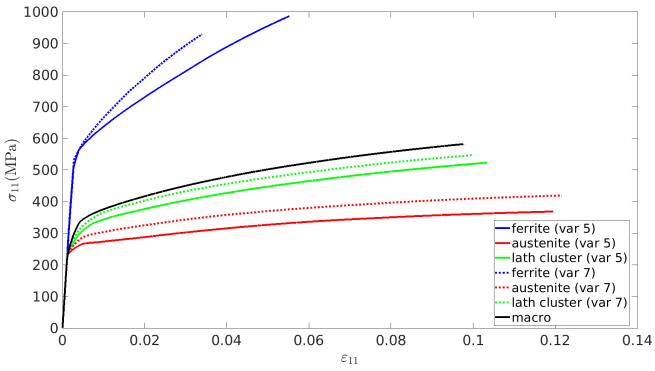

(b)

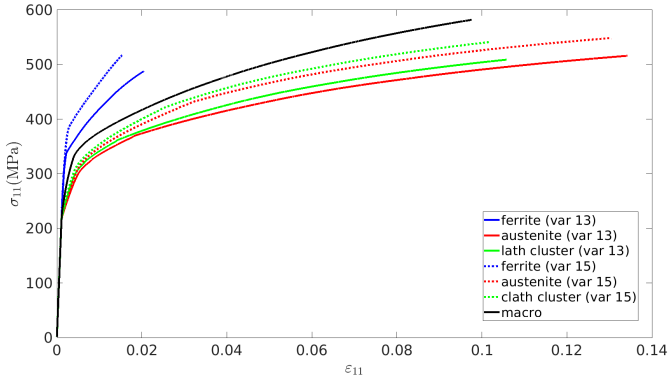

(c)

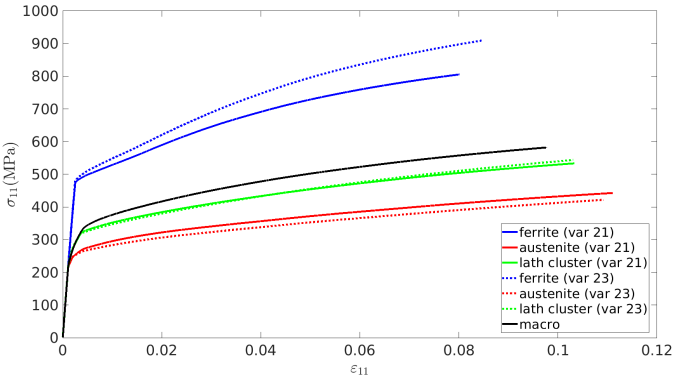

(d)

Figure 18: Stress/strain responses according to the x-direction for the *first group of variants* : (a) 1, 3 (H1, B1); (b) 5, 7 (H3, B1); (c) 13, 15 (H4, B1); (d) 21, 23 (H2,B1)

`

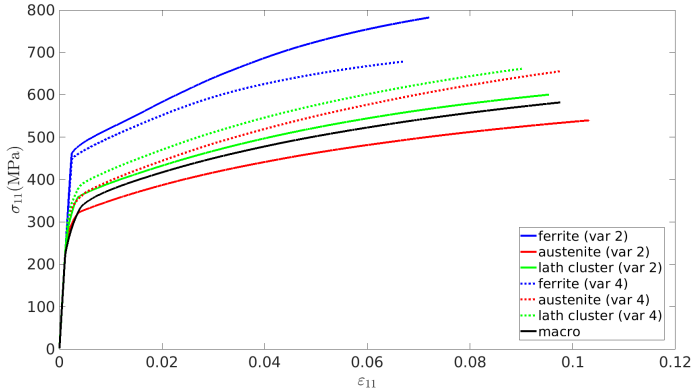

(a)

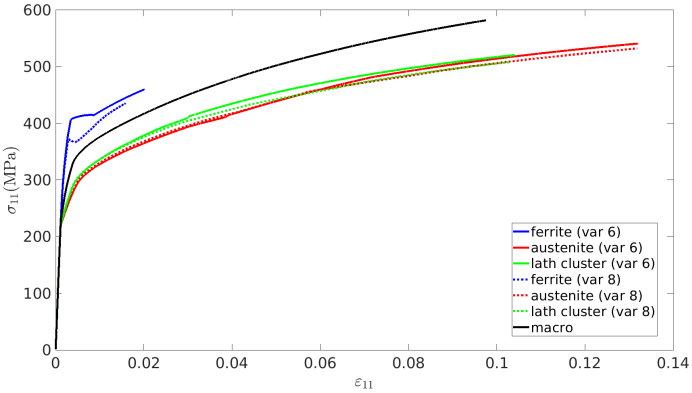

(b)

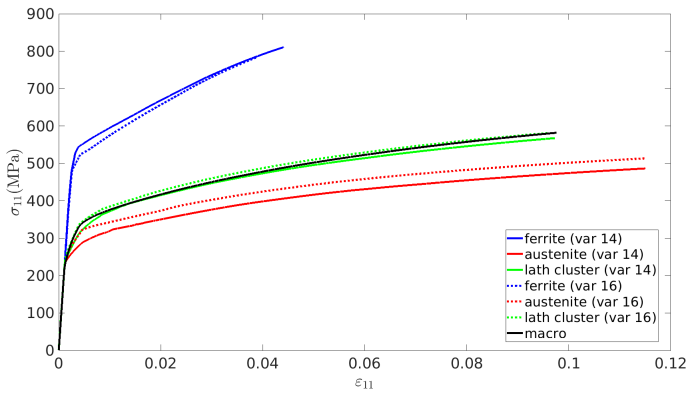

(c)

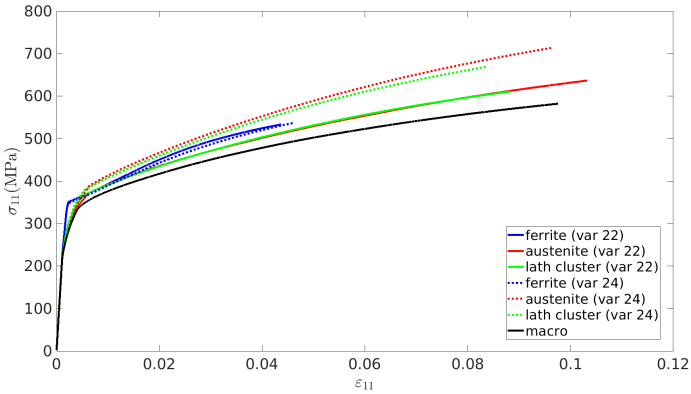

(d)

Figure 19: Stress/strain responses according to x-direction for the *second group of variants*: (a) 2, 4 (H2, B2); (b) 6, 8 (H4, B3); (c) 14, 16 (H3, B3); (d) 22, 24 (H1,B2)

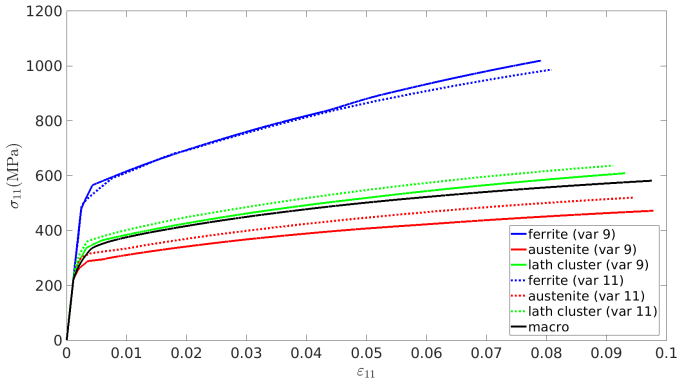

(a)

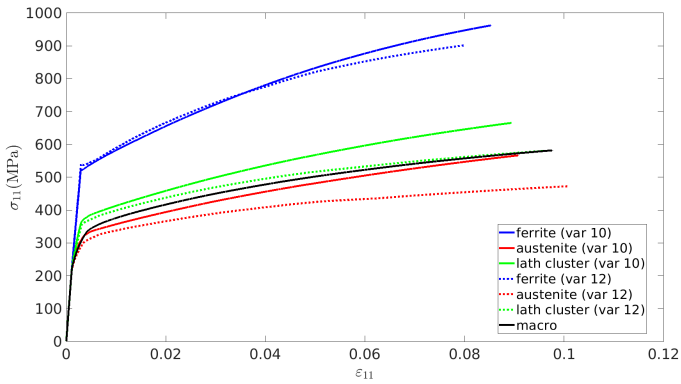

(b)

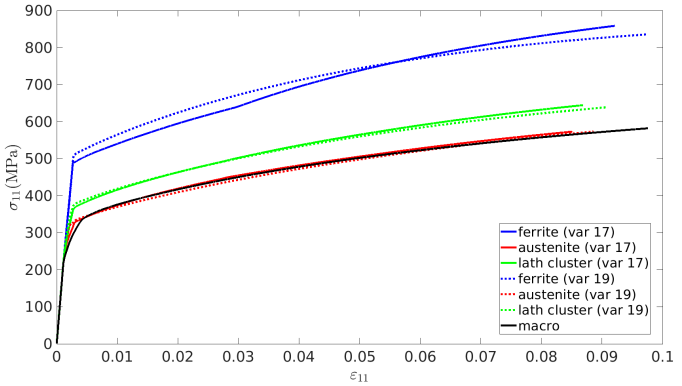

(c)

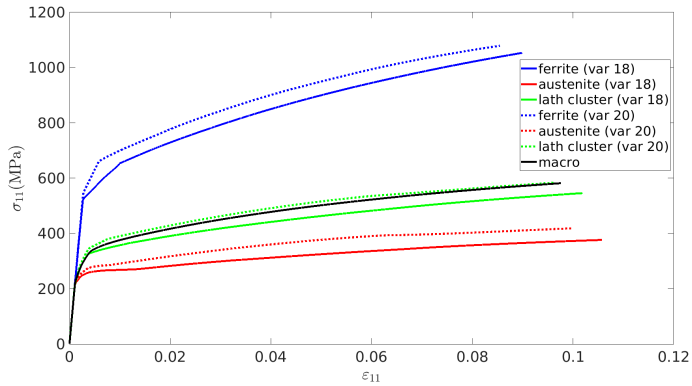

(d)

Figure 20: Stress/strain responses according to x-direction for *the third group of variants*: (a) 9, 11 (H5, B2); (b) 10, 12 (H6, B3); (c) 17, 19 (H6, B2); (d) 18, 20 (H5,B6)

4.5. Simulations of aging effects

Since the microstructure of ferrite evolves during aging, it becomes harder and more brittle, these effects can be simulated by considering different hardening parameters for ferrite only, while

assuming the same materials parameters for austenite. The materials parameters were identified using the tensile curve of the aged specimen until 6% of strain (see Figure 9b). They are reported in Table 3, for which only r_0 and q were modified for ferrite. Figure 21 displays the comparisons between stress/strain responses according to the X-direction obtained for the three groups of variants with materials parameters identified for the as-received and the aged specimen. The first group is represented by variants 1, 3 (H1, B1), see Figure 21(a,b). The second group of variants is represented by variants 2, 4 (H2, B2), see Figure 21(c,d). The third group of variants is represented by variants 9, 11 (H5, B2), see Figure 21(e,f). It is seen that aging is at the origin of an increase of the stress in ferrite. Therefore, incompatibility stresses and strains between both phases are more important in the case of the aged specimen. This trend has a consequence in the internal stresses at the different scales (see section 4.6).

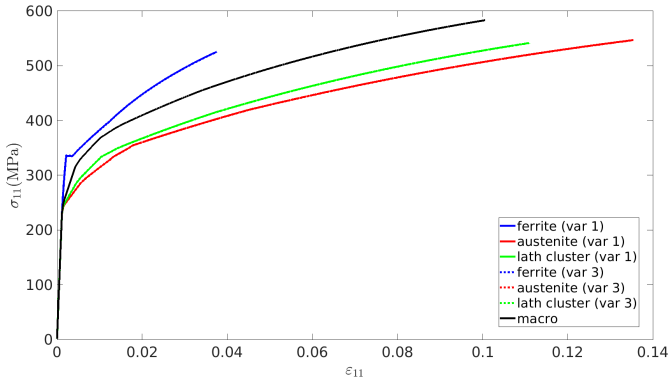

(a)

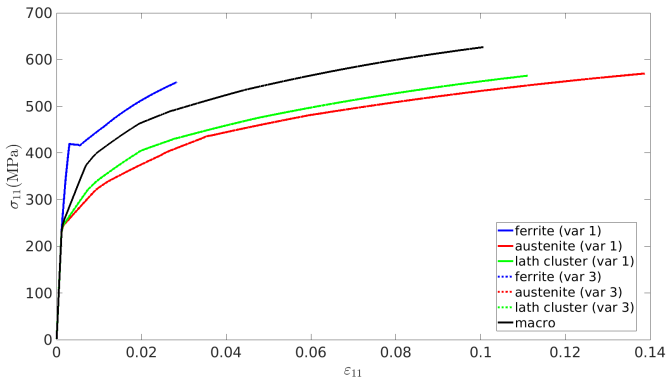

(b)

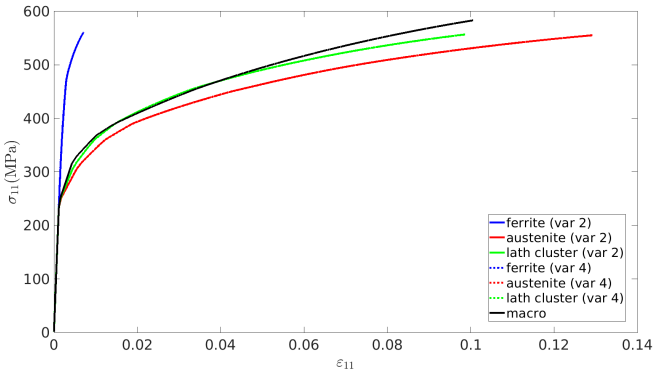

(c)

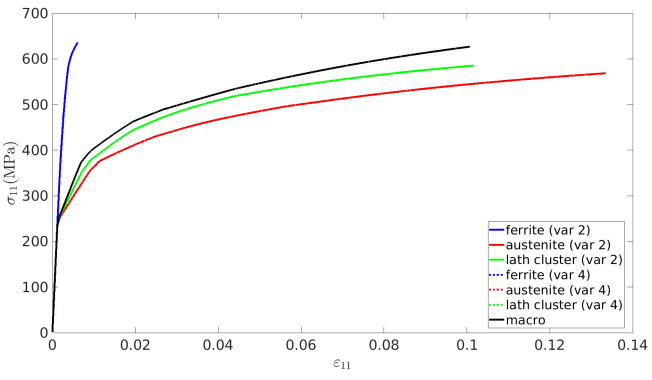

(d)

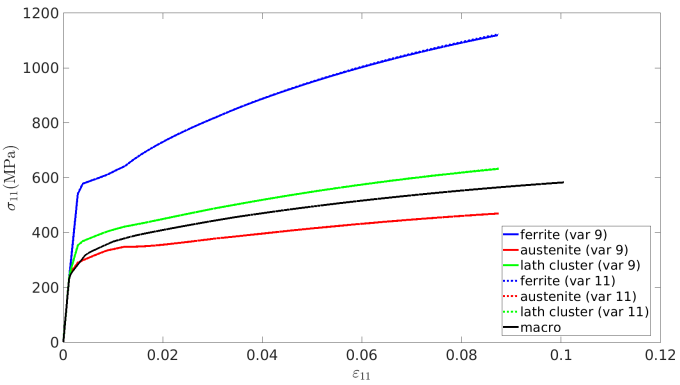

(e)

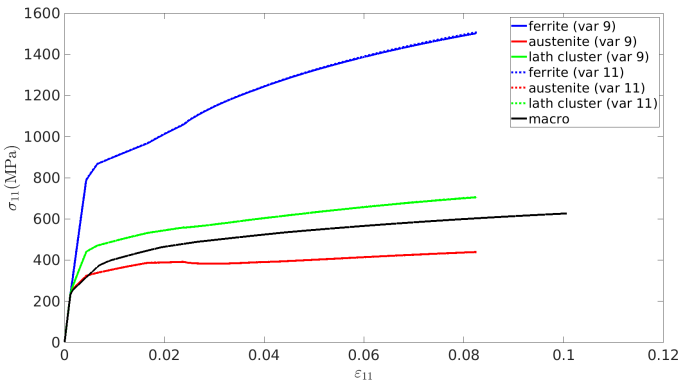

(f)

Figure 21: Comparisons between the stress/strain responses according to the X-direction obtained for the first group with variants 1, 3 (H1, B1): (a) no aging, (b) aging; for the second group with variants 2, 4 (H2, B2): (c) no aging, (d) aging; for the third group with variants 9, 11 (H5, B2): (e) no aging, (f) aging.

4.6. Bauschinger effect

Finally, let us study the respective influences of ferritic grain orientation and aging on internal stress developemnts during tension-compresssion, i.e. reverse loading. Polycrystal plasticity models are good candidates to study load reversals (see e.g. Wang et al., 2020). In this duplex steel, the development of internal stresses at the different scales is analyzed in the light of the present model to study the Bauschinger effect, which is defined as the difference in plastic flow stress after reversed deformation (Atkinson et al., 1974; Corbin et al., 1996). Such study was investigated in as received and aged duplex stainless steels by Verhaeghe et al. (1996). At the first scale, the present model does not assume intra-granular backstress (*c=d=0* in equation (30)), which would be needed to predict stabilized cycles for this alloy. This mechanism is not studied here (see Bugat, 2000). At the mesoscale, the incompatibility stresses are dependent on the HP orientation with respect to the loading direction (see Figure 12), which lead to a backstress originated from inter-phase stress accommodation. Figure 22 reports simulated cyclic responses (2 cycles) performed in tension (forward loading) and compression (reverse loading) for the aggregate of 24 KS variants (bi-crystal) and for the poly-bicrystal. Figure 22(a) and (b) compare the cyclic responses with no aging and with aging, respectively, for $\phi_1 = 0°, \phi = 0°, \phi_2 = 0°$. Figure 22(c) and (d) compare the cyclic responses with no aging and with aging, respectively, for $\phi_1 = 18.11°, \phi = 40.12°, \phi_2 = 7.52°$. Figure 22(e) and (f) compare the cyclic responses of the poly-bicrystal with no aging and with aging, respectively. Following Atkinson et al. (1974), Corbin et al. (1996) and Verhaeghe et al. (1996), the backstress (Σ_b) reflecting the Bauschinger effect is defined as $\Sigma_b = (\Sigma_f - \Sigma_r)/2$, where Σ_f is the forward flow stress at 2% of strain and Σ_r is the

reverse stress at the onset of plasticity in compression during the first cycle. The results for the simulations are gathered in Table 4. It is shown that the increase in backstress due to aging is important. This increase varies from 51 to 65 MPa, see Figures 22(b)(d)(f). The role of the ferritic grain orientation is highlighted. The cyclic curves in the elastic-plastic transitions are more rounded (see Figure 22(c) compared to Figure 22(a)) due to the larger scatter of internal stresses (see Figure 17 compared to Figure 13), and, the backstress increase is 37 MPa. This phenomenon is even more pronounced for the poly-bicrystal, where the backstress increase is equal to 73 MPa between Figure 22(a) and Figure 22(e). It is found that the largest backstress is given for the aged poly-bicrystal. These gradual increase of backstress Σ_b for each configuration is due to an increase of stress heterogeneities in both phases when upscaling from the mesoacle to macroscales.

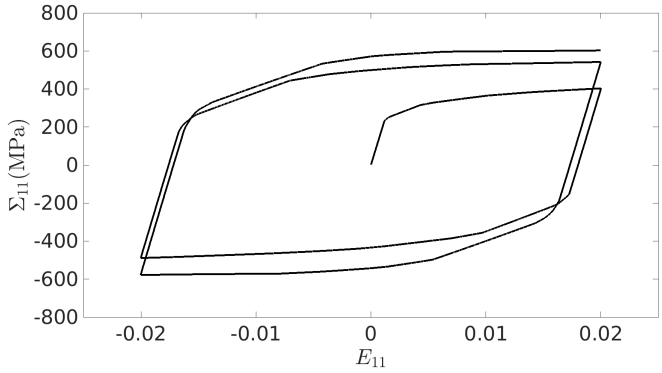

(a)

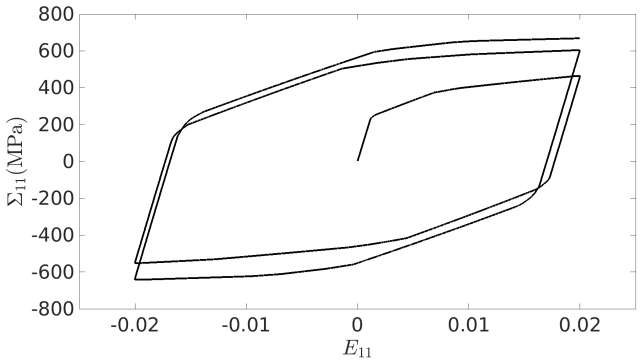

(b)

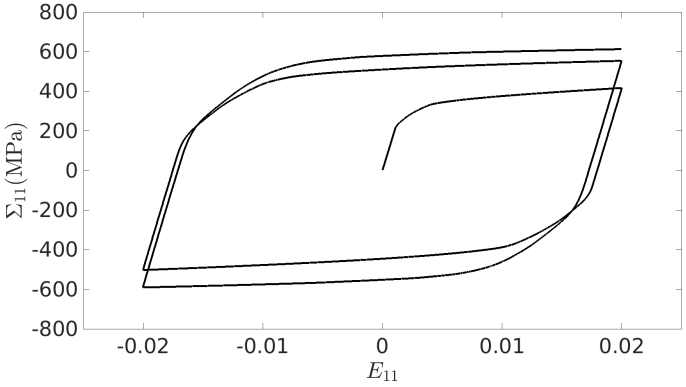

(c)

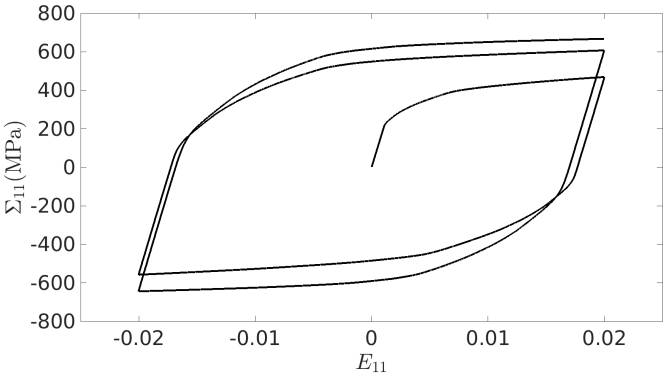

(d)

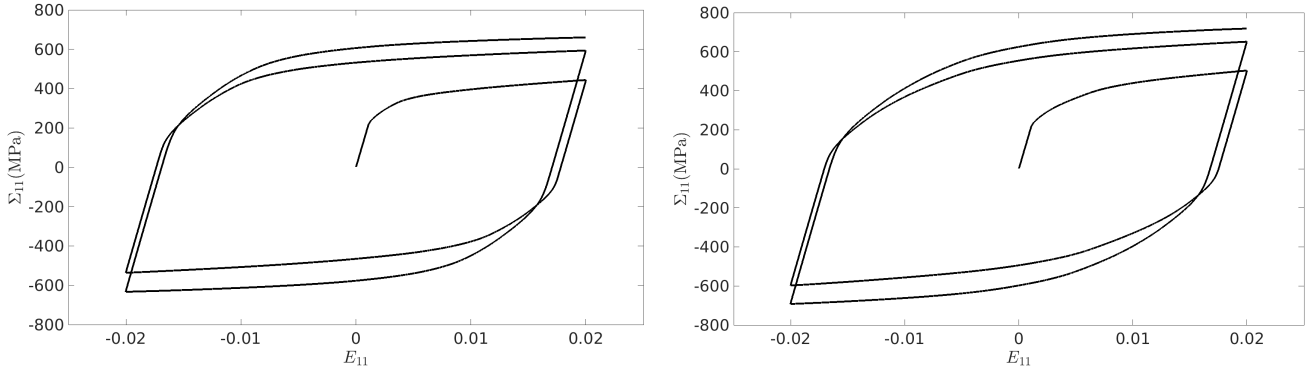

(e) (f)

Figure 22: Tension-compression cyclic responses for bi-crystal : $\phi_1 = 0°, \phi = 0°, \phi_2 = 0°$ (a) no aging, (b) aging (c); bi-crystal : $\phi_1 = 18.11°, \phi = 40.12°, \phi_2 = 7.52°$ (c) no aging (d) aging; poly-bicrystal (e) no aging, (f) aging.

Table 4. Values of forward flow stress Σ_f at 2% of strain, Σ_r reverse stress at the onset of plasticity in compression, and backstress Σ_b for the simulations of different microstructures ("bicrystal", "poly-bicrystal") with different treatments for ferrite (non-aged, aged).

Cases	Σ_f (MPa)	Σ_r (MPa)	Σ_b (MPa)
Bicrystal (24 KS variants) $\phi_1 = 0°, \phi = 0°, \phi_2 = 0°$ Non aged	397	153	122
Bicrystal (24 KS variants) $\phi_1 = 0°, \phi = 0°, \phi_2 = 0°$ Aged	464	90	187
Bicrystal (24 KS variants) $\phi_1 = 18.11°, \phi = 40.12°, \phi_2 = 7.52°$ "Non-aged"	418	100	159
Bicrystal (24 KS variants) $\phi_1 = 18.11°, \phi = 40.12°, \phi_2 = 7.52°$ Aged	465	45	210
Poly-bicrystal Non aged	439	49	195
Poly-bicrystal Aged	503	9	247

5. Conclusions

In this paper, a multiscale microstructure-based elastoviscoplastic homogenization model is presented for the first time to predict the local and the overall behavior of a CF8M alloy, which is a cast duplex stainless steel used primary loop components of Pressurized Water Reactors (PWR). Mechanical tensile tests have been performed on as received (cast) and aged (1000h, 350°C) alloy

to identify the crystal plasticity parameters based on the Méric-Cailletaud (1991a,b)'s model at the level of single austenite laths and ferrite interlayers.

The different pillars of the model detailed in section 3 were based on EBSD analyses of the microstructural data (crystallographic orientations, phase morphologies). Four different scales were reported to model the complex microstructure of the as-cast duplex steel (Mollens et al., 2022b). The present EBSD analysis reported in section 2 provide: (i) the average orientation of primary ferritic grains with sizes in the millimeter range, (ii) the crystallographic orientation of austenite considering OR (iii) information about the austenite lath morphology and interface plane orientations (habit planes). It was found that the austenite lath is characterized by a smooth orientation spread and results from a displacive transformation according to a close {110}α habit plane (HP). The KS-OR is approximately satisfied with the surrounding ferritic grain. Therefore, a cluster of adjacent austenite laths, separated by layers of primary ferrite was modeled by a two-phase LS. At the scale of the primary ferritic grain, we considered an EVPSC scheme (Mareau and Berbenni, 2015) with 24 spherical domains containing the two-phase laminate structures corresponding to the 24 possible equiprobable KS-OR variants. This specific microstructure was called "bicrystal". Finally, the last scale defines the whole microstructure constituted of different primary ferrite grains, called "poly-bicrystal", and modeled with the same EVPSC scheme.

The main conclusions of the simulation results reported in section 4 are the following:

- The model is able to describe the average mechanical fields (stress and strain fields) at the different scales of the duplex steel microstructure: (i) in the austenite laths and in the ferrite interlayer related with a KS-OR, (ii) at the level of a cluster of austenite laths in the two-phase LS structure, (iii) at the level of primary ferritic grains ("bicrystals"), (iv) at the level of an ensemble of primary ferritic grains ("poly-bicrystals").
- The morphology due to the cluster of austenite laths is responsible for a strong anisotropic behavior observed from the mechanical responses of LS structure satisfying a pure KS-OR. This trend was confirmed with comparisons with FFT simulations with same crystal plasticity laws. The slip analysis confirms the important effects of incompatibility stresses dependent on the local configuration defined by the HP and the tensile directions. Generally, the individual responses of both phases are not sufficient to represent the stress/strain responses of the LS structure, except for the case where the loading direction is parallel the $[1\,1\,1]\alpha$ crystallographic direction in ferrite.
- In the case where the tensile loading is performed according to the $[1\,0\,0]\alpha$ crystallographic direction in ferrite, it is found that the tensile stresses in ferrite for the "bicrystal" strongly depends on the HP (among the 6 different HP), where we have identified 3 groups of KS

variants with similar mechanical behavior. The effect of primary ferritic grain crystallographic orientation is important and changes the stress state in ferrite for the different variants belonging to the three above identified groups. It was observed that stress heterogeneities are more pronounced inside the primary ferritic grain.

- The effect of aging was discussed assuming that the microstructure of ferrite has changed, affecting the intra-granular isotropic hardening parameters of ferrite. These parameters were identified using the tensile stress/strain curve for the aged specimen. Then, aging was found to enhance the mechanical contrast between both phases and increase the incompatibility stresses.
- Finally, the Bauschinger effect was studied for “bicrystal” and “poly-bicrystal” with and without aging for cyclic tension-compression loading. It was shown that even though the model does not incorporate intra-granular kinematical hardening, the model displays a backstress which depends on ferritic grain orientation and aging. The largest backstress is found for the aged “poly-bicrystal”.

Some interesting challenges remain to do with the present developed multiscale model. First, we will aim to perform some predictions in comparison to *in situ* mechanical tests extracting kinematical strain fields (*in situ* Digital Image Correlation, see e.g. Guéry et al., 2016) or lattice strain evolution in the elastoplastic transition (*in situ* X-Ray diffraction, see e.g. Wang et al., 2016; Gadalinska et al., 2020). Bauschinger tests on cast and aged specimen can be performed to validate the model parameters to predict the backstress in the light of the new model. The stresses in ferrite predicted by the model as well as slip activities can be used to predict damage initiation during aging. Lastly, the present micromechanical model will be incorporated in structural FE-based calculations using the MFront code generator (Helfer et al. 2015).

Acknowledgments

The authors thank the MAI-SN (Materials Aging Institute – Scientific Network) for financial support. Fruitful discussions with Maxime Mollens (EDF R&D), Stéphane Roux (ENS Paris Saclay), Lionel Germain (LEM3) are acknowledged.

Appendix

Table A.1: Averaged orientations (Euler-Bunge angles) of reconstructed ferritic grains from EBSD maps.

Primary ferritic grains	ϕ_1 (°)	ϕ(°)	ϕ_2(°)
1*	18.11	40.12	7.52
2	25.86	35.40	46.27
3	150.47	9.73	0.61
4	106.38	20.88	75.83
5	140.37	32.08	66.45
6	190.89	44.42	51.02
7	178.52	42.59	28.43
8	195.83	40.65	43.53
9	109.88	36.43	19.41
10	195.21	15.2	40.48
11	353.19	8.85	356.26
12	229.57	41.94	40.62
13	89.43	33.77	60.68
14	177.31	24.8	8.22
15	319.43	39.12	58.27

*: largest grain used for simulation of the bicrystal.

Table A.2. List of the 24 cubic symmetry group matrices used to generate the 24 KS variants in Table 2.

Variant Number	Cubic symmetry group matrices
V1	$\begin{bmatrix}1 & 0 & 0\\ 0 & 1 & 0\\ 0 & 0 & 1\end{bmatrix}$
V2	$\begin{bmatrix}0 & -1 & 0\\ 1 & 0 & 0\\ 0 & 0 & 1\end{bmatrix}$
V3	$\begin{bmatrix}-1 & 0 & 0\\ 0 & -1 & 0\\ 0 & 0 & 1\end{bmatrix}$
V4	$\begin{bmatrix}0 & 1 & 0\\ -1 & 0 & 0\\ 0 & 0 & 1\end{bmatrix}$
V5	$\begin{bmatrix}1 & 0 & 0\\ 0 & 0 & -1\\ 0 & 1 & 0\end{bmatrix}$
V6	$\begin{bmatrix}0 & -1 & 0\\ 0 & 0 & -1\\ 1 & 0 & 0\end{bmatrix}$
V7	$\begin{bmatrix}-1 & 0 & 0\\ 0 & 0 & -1\\ 0 & -1 & 0\end{bmatrix}$
V8	$\begin{bmatrix}0 & 1 & 0\\ 0 & 0 & -1\\ -1 & 0 & 0\end{bmatrix}$

V9	$\begin{bmatrix} 0 & 0 & 1 \\ 1 & 0 & 0 \\ 0 & 1 & 0 \end{bmatrix}$
V10	$\begin{bmatrix} 0 & 0 & 1 \\ 0 & -1 & 0 \\ 1 & 0 & 0 \end{bmatrix}$
V11	$\begin{bmatrix} 0 & 0 & 1 \\ -1 & 0 & 0 \\ 0 & -1 & 0 \end{bmatrix}$
V12	$\begin{bmatrix} 0 & 0 & 1 \\ 0 & 1 & 0 \\ -1 & 0 & 0 \end{bmatrix}$
V13	$\begin{bmatrix} -1 & 0 & 0 \\ 0 & 0 & 1 \\ 0 & -1 & 0 \end{bmatrix}$
V14	$\begin{bmatrix} 0 & 1 & 0 \\ 0 & 0 & 1 \\ 1 & 0 & 0 \end{bmatrix}$
V15	$\begin{bmatrix} 1 & 0 & 0 \\ 0 & 0 & 1 \\ 0 & -1 & 0 \end{bmatrix}$
V16	$\begin{bmatrix} 0 & -1 & 0 \\ 0 & 0 & 1 \\ -1 & 0 & 0 \end{bmatrix}$
V17	$\begin{bmatrix} 0 & 0 & -1 \\ -1 & 0 & 0 \\ 0 & 1 & 0 \end{bmatrix}$
V18	$\begin{bmatrix} 0 & 0 & -1 \\ 0 & 1 & 0 \\ 1 & 0 & 0 \end{bmatrix}$
V19	$\begin{bmatrix} 0 & 0 & -1 \\ 1 & 0 & 0 \\ 0 & -1 & 0 \end{bmatrix}$
V20	$\begin{bmatrix} 0 & 0 & -1 \\ 0 & -1 & 0 \\ -1 & 0 & 0 \end{bmatrix}$
V21	$\begin{bmatrix} 1 & 0 & 0 \\ 0 & -1 & 0 \\ 0 & 0 & -1 \end{bmatrix}$
V22	$\begin{bmatrix} 0 & 1 & 0 \\ 1 & 0 & 0 \\ 0 & 0 & -1 \end{bmatrix}$
V23	$\begin{bmatrix} -1 & 0 & 0 \\ 0 & 1 & 0 \\ 0 & 0 & -1 \end{bmatrix}$
V24	$\begin{bmatrix} 0 & -1 & 0 \\ -1 & 0 & 0 \\ 0 & 0 & -1 \end{bmatrix}$

Table A.3. The 12 slip systems in the f.c.c. structure with Schmid and Boas's notation (1968).

Notation	Crystallographic plane	Crystallographic direction
A2	$(\bar{1}\ 1\ 1)$	$[0\ \bar{1}\ 1]$
A3	$(\bar{1}\ 1\ 1)$	$[1\ 0\ 1]$
A6	$(\bar{1}\ 1\ 1)$	$[1\ 1\ 0]$
B2	$(1\ 1\ 1)$	$[0\ \bar{1}\ 1]$
B4	$(1\ 1\ 1)$	$[\bar{1}\ 0\ 1]$
B5	$(1\ 1\ 1)$	$[\bar{1}\ 1\ 0]$
C1	$(\bar{1}\ \bar{1}\ 1)$	$[0\ 1\ 1]$
C3	$(\bar{1}\ \bar{1}\ 1)$	$[1\ 0\ 1]$
C5	$(\bar{1}\ \bar{1}\ 1)$	$[\bar{1}\ 1\ 0]$
D1	$(1\ \bar{1}\ 1)$	$[0\ 1\ 1]$
D4	$(1\ \bar{1}\ 1)$	$[\bar{1}\ 0\ 1]$
D6	$(1\ \bar{1}\ 1)$	$[1\ 1\ 0]$

Table A.4. The 12 slip systems in the b.c.c. structure with their notations according to Le et al. (2020).

Notation	Crystallographic plane	Crystallographic direction
2A	$(0\ \bar{1}\ 1)$	$[\bar{1}\ 1\ 1]$
3A	$(1\ 0\ 1)$	$[\bar{1}\ 1\ 1]$
6A	$(1\ 1\ 0)$	$[\bar{1}\ 1\ 1]$
2B	$(0\ \bar{1}\ 1)$	$[1\ 1\ 1]$
4B	$(\bar{1}\ 0\ 1)$	$[1\ 1\ 1]$
5B	$(\bar{1}\ 1\ 0)$	$[1\ 1\ 1]$
1C	$(0\ 1\ 1)$	$[\bar{1}\ \bar{1}\ 1]$
3C	$(1\ 0\ 1)$	$[\bar{1}\ \bar{1}\ 1]$
5C	$(\bar{1}\ 1\ 0)$	$[\bar{1}\ \bar{1}\ 1]$
1D	$(0\ 1\ 1)$	$[1\ \bar{1}\ 1]$
4D	$(\bar{1}\ 0\ 1)$	$[1\ \bar{1}\ 1]$
6D	$(1\ 1\ 0)$	$[1\ \bar{1}\ 1]$

References

Atkinson, J.D., Brown, L.M., Stobbs, W.M., 1974. The work-hardening of copper-silica. IV. The Bauschinger effect and plastic relaxation, Philos. Mag. 30, 1247-1280 (doi: doi.org/10.1080/14786437408207280)

Auger, P., Danoix, F., Menand, A., Bonnet, S., Bourgoin, J., Guttmann, M., 1990. Atom probe and transmission electron microscopy study of aging of cast duplex stainless steels. Mater. Sci. Tech. 6(3), 301-313, 1743-2847 (doi: 10.1179/mst.1990.6.3.301)

Baczmanski, A., Zhao, Y., Gadalinska, E., Le Joncour, L., Wronski, S., Braham, C., Panicaud, B., François, M., Buslaps, T., Soloducha, K., 2016. Elastoplastic deformation and damage process in duplex stainless steels studied using synchrotron and neutron diffractions in comparison with a self-consistent model, Int. J. Plast. 81, 102-122. (doi: 10.1016/j.ijplas.2016.01.018)

Badyka, R., Monnet, G., Saillet, S., Domain, C., Pareige, C., 2019. Quantification of hardening contribution of G-Phase precipitation and spinodal decomposition in aged duplex stainless steel: APT analysis and micro-hardness measurements, J. Nucl. Mater. 514, 266-275 (doi: 10.1016/j.jnucmat.2018.12.002)

Berbenni, S., Capolungo, L., 2015. A Mori-Tanaka homogenization scheme for non-linear elasto-viscoplastic heterogeneous materials based on Translated Fields: an “affine” extension. Comptes Rendus de Mécanique 343, 95-106 (doi: 10.1016/j.crme.2014.12.003)

Berbenni, S., Paliwal, B., Cherkaoui, M., 2013. A micromechanics-based model for shear-coupled grain boundary migration in bicrystals. Int. J. Plast. 44, 68-94 (doi: 10.1016/j.ijplas.2012.11.011)

Berbenni, S., 2021. A time-incremental homogenization method for elasto-viscoplastic particulate composites based on a modified secant formulation Int. J. Solids Struct. 229,111136 (doi: 10.1016/j.ijsolstr.2021.111136)

Berveiller, M., Zaoui, A., 1979. An extension of the self-consistent scheme to plastically-flowing polycrystals. J. Mech. Phys. Solids 26, 325-344 (doi: 10.1016/0022-5096(78)90003-0)

Bethmont, M., Meyzaud, Y., Soulat, P.,1996. Properties of cast austenitic materials for light water reactors. Fracture in Austenitic Components, 65(3):221–229 (doi: 10.1016/0308-0161(94)00133-4)

Bonnet, S., Bourgoin, J., Champredonde, J., Guttmann, D., Guttmann, M., 1990. Relationship between evolution of mechanical properties of various cast duplex stainless steels and metallurgical and aging parameters: outline of current EDF programmes. Mater. Sci. Tech. 6(3), 221–229 (doi: 10.1179/mst.1990.6.3.221)

Brassard, L., Stainier, L., Doghri, I., Delannay, L., 2012. Homogenization of elasto(visco)plastic composites based on an incremental variational principle. Int. J. Plast. 36, 86-112 (doi : 10.1016/j.ijplas.2012.03.010)

Bugat, S., Comportement et endommagement des aciers austéno-ferritiques vieillis : une approche micromécanique. Ph.D. thesis. Ecole Nationale Supérieure des Mines de Paris, France, 2000.

Bugat, S., Besson, J., Pineau, A. 1999. Micromechanical modeling of the behavior of duplex stainless steels. Comp. Mater. Sci. 16, 158-166 (doi :10.1016/S0927-0256(99)00058-0)

Bugat, S., Besson, J., Gourgues, A. F., N'Guyen, F., Pineau, A., 2001. Microstructure and damage initiation in duplex stainless steels. Mater. Sci. Eng. A 317, 32-36 (doi : 10.1016/S0921-5093(01)01196-0)

Caillletaud, G., Pilvin, P., 1994. Utilisation de modèles polycristallins pour le calcul élements finis. Revue Européennes des Élements Finis 3(4), 515-541 (doi: 10.1080/12506559.1994.10511147)

Charles, J., 2009. Corrosion Resistance Properties. In Duplex Stainless Steels, pages 47–114. John Wiley & Sons, Ltd. ISBN 978-1-118-55799-0 (doi: 10.1002/9781118557990.ch2)

Coudon, F., Cailletaud, G., Cormier, J., Marcin, L., 2019. A multiscale model for nickel-based directionally solidified materials. Int. J. Plast. 115, 1-17 (doi: 10.1016/j.ijplas.2018.10.003).

Corbin, S.F., Wilkinson, D.S., Embury, J.D. 1996. The Bauschinger effect in a particulate reinforced Al alloy, Mater. Sci. Eng. A 207, 1-11 (doi: 10.1016/0921-5093(95)10028-8)

Das, S., Ponte Castañeda, P., 2021. Differential variational estimates for the macroscopic response and field statistics of elasto-viscoplastic polycrystals. J. Mech. Phys. Solids 147, 104202 (doi: 10.1016/j.jmps.2020.104202).

Devillers-Guerville, L., 1998. Rupture d'aciers inoxydables austéno-ferritiques moulés, fragilisés par vieillissement à 350-400°C : aspects microstructuraux – simulation numérique de la dispersion et des effets d'échelle. Ph.D. thesis, Ecole Nationale Supérieure des Mines de Paris.

Dodla, S., Bertram, A., Krüger, M., 2015. Finite element simulation of lamellar copper-silver composites. Comput. Mater. Sci. 101, 29-38 (doi:10.1016/j.commatsci.2015.01.012)

Doghri, I., Adam, L., Bilger, N., 2010. Mean-field homogenization of elastoviscoplastic composites based on a general incrementally affine linearization method. Int. J. Plast. 26, 219-223 (doi: 10.1016/j.ijplas.2009.06.003)

El Omri, A., Fennan, A., Sidoroff, F., Hihi, A. 2000. Elastic-plastic homogenization for layered composites. Eur. J. Mech. A/Solids 19, 585-601 (doi: 10.1016/S0997-7538(00)00182-0)

Eshelby, J.D., 1957. The determination of the elastic field of an ellipsoidal inclusion, and related problems. Proc. R. Soc. Lond. Math. Phys. Eng. Sci. 241, 376-396 (doi: 10.1098/rspa.1957.0133)

Flipon, B., Keller, C., Quey, R., Barbe, F. 2020. A full-field crystal-plasticity analysis of bimodal polycrystals. Int. J. Solids Struct. 184, 178-192 (doi: 10.1016/j.ijsolstr.2019.02.005)

Fournier, B., Sauzay, M., Pineau, A., 2011. Micromechanical model of the high temperature cyclic behavior of 9-12%Cr martensitic steels. Int. J. Plast. 27, 1803-1816 (doi:10.1016/j.ijplas.2011.05.007)

Franciosi, P., Berbenni, S., 2008. Multi-laminate plastic-strain organization for non-uniform TFA modeling of poly-crystal regularized plastic flow. Int. J. Plast. 24, 1549-1580 (doi: 10.1016/j.ijplas.2007.12.004)

Gadalinska, E., Baczmanski, A., Braham, C., Gonzalez, G., Sidhom, H., Wronski, S., Buslaps, T., Wierbanowski, K., 2020. Stress localisation in lamellar cementite and ferrite during elastoplastic deformation of pearlitic steel studied using diffraction and modelling. Int. J. Plast. 127, 102651 (doi: 10.1016/j.ijplas.2019.102651)

Guery, A., Hild, F., Latourte, F., Roux, S., 2016. Slip activities in polycrystals determined by coupling DIC measurements with crystal plasticity calculations. Int. J. Plast. 81, 249-266 (doi: 10.1016/j.ijplas.2016.01.008)

Haghdadi, N., Cizek, P., Hodgson, P.D., Tari, V., Rohrer, G.S., Beladi, H., 2018. Effect of ferrite-to-austenite phase transformation path on the interface crystallographic character distributions in a duplex stainless steel. Acta Mater. 145, 196-209 (doi: 10.1016/j.actamat.2017.11.057)

Helfer, T., Michel, B., Proix, J.-M., Salvo M., Sercombe, J., Casella, M., 2015. Introducing the open-source MFront code generator: Application to mechanical behaviours and material knowledge management within the PLEIADES fuel element modelling platform. Comp. Math. Appl. 70(5), 994-1023 (doi: 10.1016/j.camwa.2015.06.027).

Hill, R., 1965. Continuum micro-mechanics of elastoplastic polycrystals. J. Mech. Phys. Solids 13, 89-101 (doi: 10.1016/0022-5096(65)90023-2)

Jeong, Y., Tomé, C.N., 2020. An efficient elasto-visco-plastic self-consistent formulation: Application to steel subjected to loading path changes. Int. J. Plast. 135, 102812 (doi: 10.1016/j.ijplas.2020.102812)

Kasemer, M., Dawson, P., 2020. A finite element methodology to incorporate kinematic activation of discrete deformation twins in a crystal plasticity framework. Comp. Methods Appl. Mech. Engrg. 358, 112653 (doi: 10.1016/j.cma.2019.112653)

Kowalczyk-Gajewska K. 2011. Micromechanical model of polycrystalline materials with lamellar substructure. Arch. Metal. Mater. 56(2), 509-522 (doi: 10.2478/v10172-011-0055-3)

Kröner, E., 1990. Modified green functions in the theory of heterogeneous and/or anisotropic linearly elastic media. In: Weng, G.J., Taya, M., Abé, H. (Eds.), Micromechanics and Inhomogeneity: the Toshio Mura 65th Anniversary Volume. Springer New York, New York, NY, pp. 197–211. (doi: 10.1007/978-1-4613-8919-4_13)

Lahellec, N., Suquet, P., 2007. On the effective behavior of non linear inelastic composites: I. Incremental variational principles. J. Mech. Phys. Solids 55, 1932-1963 (doi: 10.1016/j.jmps.2007.02.003)

Lahellec, N., Suquet, P., 2013. Effective response and field statistics in elasto-plastic and elasto-viscoplastic composites under radial and non radial loadings. Int. J. Plast. 42, 1-30. (doi: 10.1016/j.ijplas.2012.09.005)

Lhadi S., Berbenni, S., Gey, N., Richeton, T., Germain, L., 2018. Micromechanical modeling of the effect of elastic and plastic anisotropies on the mechanical behavior of β-Ti alloys, Int. J. Plast. 109, 88-107 (doi: 10.1016/j.ijplas.2018.05.010)

Lhadi, S., Purushottam raj purohit, R. R. P., Richeton, T., Gey, N., Berbenni, S., Perroud, O., Germain, L. 2020. Elasto-viscoplastic tensile behavior of as-forged Ti-1023 alloy: Experiments and micromechanical modeling. Mater. Sci. Eng. A 787, 139491 (doi: doi.org/10.1016/j.msea.2020.13949)

Lebensohn, R.A., Canova, G.R., 1997. A self-consistent approach for modelling texture development of two-phase polycrystals: application to titanium alloys. Acta Mater. 45 (9), 3687-3694 (doi: 10.1016/S1359-6454(97)00067-0)

Lebensohn, R.A., 1999. Modelling the role of local correlations in polycrystal plasticity using viscoplastic self-consistent schemes. Modell. Simul. Mater. Sci. Eng. 7, 739-746 (doi.org/10.1088/0965-0393/7/5/306)

Lebensohn, R.A., Kanjarla, A.K., Eisenlohr, P., 2012. An elasto-viscoplastic formulation based on fast fourier transforms for the prediction of micromechanical fields in polycrystalline materials. Int. J. Plast. 32-33, 59-69 (doi.org/10.1016/j.ijplas.2011.12.005)

Le, L.T., Ammar, K., Forest, S., 2020. Efficient simulation of single and poly-crystal plasticity based on the pencil glide mechanism. C. R. Méca. 348 (10-11), 847-876 (doi: 10.5802/crmeca.44)

Le Delliou, P., Saillet, S., 2015. Integrity and Life Assessment of Cast Duplex Stainless Steel Elbows of EDF PWR Main Coolant Piping. In : Volume 7: Operations, Applications and Components, page V007T07A014. American Society of Mechanical Engineers, Boston, Massachusetts, USA (doi: 10.1115/PVP2015-45231)

Li, J., Romero, I., Segurado, J., 2019. Development of a thermo-mechanically coupled crystal plasticity modeling framework: Application to polycrystalline homogenization. Int. J. Plast. 119, 313-330 (doi : 10.1016/j.ijplas.2019.04.008)

Magnin, T., Moret, F., 1982. Mechanical twinning in ferritic stainless steels. Scripta Metall., 16(11), 1225-1228 (doi: 10.1016/0036-9748(82) 90471-9)

Mareau, C., Berbenni, S., 2015. An affine formulation for the self-consistent modeling of elasto-viscoplastic heterogeneous materials based on the translated field method. Int. J. Plast. 64, 134-150 (doi: 10.1016/j.ijplas.2014.08.011)

Masson, R., Bornert, M., Suquet, P., Zaoui, A., 2000. Affine formulation for the prediction of the effective properties of nonlinear composites and polycrystals. J. Mech. Phys. Solids 48, 1203-1227 (doi: 10.1016/S0022-5096(99)00071-X)

Masson, R., Seck, M.E.B., Fauque, J., Garajeu, M., 2020. A modified secant formulation to predict the overall behavior of elasto-viscoplastic particulate composites. J. Mech. Phys. Solids 137, 103874 (doi: 10.1016/j.jmps.2020.103874)

M'Cirdi, L., Comportement et eendommagement sous sollicitation mécanique d'un acier austéno-ferritique moulé vieilli. Ph.D. thesis. Ecole Nationale Supérieure d'Arts et Métiers, Paris, France, 2000.

M'Cirdi, L., Lebrun, J.L., Inal, K., Barbier, G., 2001. Experimental approach of a crystallographic cleavage criterion in a cast aged duplex stainless steel. Acta Mater. 49, 3879-3887 (doi : 10.1016/S1359-6454(01)00249-X)

Mercier, S., Molinari, A., Berbenni, S., Berveiller, M., 2012. Comparison of different homogenization approaches for elastic–viscoplastic materials. Modell. Simul. Mater. Sci. Eng. 20, 024004 (doi: 10.1088/0965-0393/20/2/024004)

Mercier, S., Molinari, A., 2009. Homogenization of elastic-viscoplastic heterogeneous materials: self-consistent and Mori-Tanaka schemes. Int. J. Plast. 25, 1024-1048 (doi: 10.1016/j.ijplas.2008.08.006).

Méric, L., Cailletaud, G., 1991a. Single crystal modeling for structural calculations: Part 1 – Model presentation. ASME J. Eng. Mater. Tech. 113, 162-170 (doi: 10.1115/1.2903374)

Méric, L., Cailletaud, G., 1991b. Single crystal modeling for structural calculations: Part 2 – Finite element implementation. ASME J. Eng. Mater. Tech. 113, 171-182 (doi :10.1115/1.2903375)

Michaud, W.F., Toben, P.T., Soppet, W. K., Chopra, O.K., 1994. Tensile Property Characterization of Thermally Aged Cast Stainless Steels. Technical Report. NUREG/CR-6142, ANL-93/35.

Molinari, A., Ahzi, S., Kouddane, R., 1997. On the self-consistent modeling of elastic-plastic behavior of polycrystals. Mech. Mater. 26, 43-62 (doi.org/10.1016/S0167-6636(97)00017-3)

Mollens, M., 2022a. Modélisation multi-échelle du comportement mécanique d'un acier austéno-ferritique vieilli thermiquement. PhD thesis. Ecole Normale Supérieure Paris Saclay, 2022

Mollens, M., Roux, S., Hild, F., Guery, A., 2022b. Insights into a dualphase steel microstructure using EBSD and image-processing-based workflow. J. Appl. Crystal. 55(3):601–610. (doi: 10.1107/S1600576722004265)

Mollens, M., Guery, A., Loisnard, D., Hild, F., Roux, S., 2022c. Link between BCC-FCC orientation relationship and austenite morphology in CF8M stainless steel. submitted.

Nye, J.F., 1957. Physical properties of crystals. Clarendon Press, Oxford.

Paquin, A., Sabar, H., Berveiller, M., 1999. Integral formulation and self-consistent modelling of elastoviscoplastic behavior of heterogeneous materials. Arch. Appl. Mech. 69, 14-35 (doi: 10.1007/s004190050201).

Paquin, A., Berbenni, S., Favier, V., Lemoine, X., Berveiller, M, 2001. Micromechanical modeling of the elastic-viscoplastic behavior of polycrystalline steels. Int. J. Plast. 17, 1267-1302 (doi: 10.1016/S0749-6419(00)00047-4)

Pareige, C., Emo, J., Saillet, S., Domain, C., Pareige, P., 2015. Kinetics of G-phase precipitation and spinodal decomposition in very long aged ferrite of a Mo-free duplex stainless steel. J. Nucl. Mater. 465, 383-389 (doi: 10.1016/j.jnucmat.2015.06.017)

Qu, J., Cherkaoui, M., 2006. Fundamentals of micromechanics of solids. John Wiley & Sons, 2006.

Richeton, T., Berbenni, S., 2013. Effects of heterogeneous elasticity coupled to plasticity on stresses and lattice rotations in bicrystals: A Field Dislocation Mechanics viewpoint. Eur. J. Mech. A/Solids 3, 231-247 (doi: 10.1016/j.euromechsol.2012.06.010)

Richeton, T., 2022. Stress partitioning and effective behavior of N-phase laminates in anisotropic elasticity from a fast explicit method. J. Theor. Comp. Appl. Mech., March 2022. (doi:10.46298/jtcam.8506)

Riyad, I.A., Feather, W.G., Vasilev, E., Lebensohn, R., McWilliams, B.A., Pilchak, A.L., Knecevic, M., 2021. Modeling the role of local crystallographic correlations in microstructures of Ti-6Al-4V using a correlated structure visco-plastic self-consistent polycrystal plasticity formulation. Acta Mater. 203, 116502 (doi: 10.1016/j.actamat.2020.116502).

Roos, A., Chaboche, J.-L., Gélébart, L., Crépin, J., 2004. Multiscale modelling of titanium aluminides. Int. J. Plast. 20, 811-830 (doi: 10.1016/j.ijplas.2003.08.005)

Roters, F., Eisenlohr, P., Hantcherli, L., Tjahjanto, D. D., Bieler, T.R., Raabe, D., 2010. Overview of constitutive laws, kinematics, homogenization and multiscale methods in crystal plasticity finite-element modeling: Theory, experiments, applications. Acta Mater. 58 (2010) 1152-1211 (doi: 10.1016/j.actamat.2009.10.058)

Schmid, E., Boas, W. 1968. Plasticity of crystals with special reference to metals. Chapman & Hall.

Sigmund, T., Werner, E., Fischer, F.D., 1995. On the thermomechanical deformation behavior of duplex-type materials. J. Mech. Phys. Solids 43, 495-532 (doi: 10.1016/0022-5096(95)00003-2)

Solomon, H.D., Devine, T.M., 1982. Duplex stainless steels: a tale of two phases. American Society for Metals.

Song, P., Ji, Y., Chen, L., Liu, W., Zhang, C., Chen, L.Q., Zhigang, Y., 2016. Phase-field simulation of austenite growth behavior: Insights into the austenite memory phenomenon. Comp. Mater. Sci. 117, 139-150 (doi: 10.1016/j.commatsci.2016.01.030)

Stupkiewicz, S., Petryk, H., 2002. Modelling of laminated microstructures in stress-induced martensitic transformations. J. Mech. Phys. Solids 50, 2303-2331 (doi: 10.1016/S0022-5096(02)00029-7)

Taylor, G.I., 1938. Plastic strain in metals. J. Inst. Metals 61, 307–324.

Tiba, I., Richeton, T., Motz, C., Vehoff, H., Berbenni, S., 2015. Incompatibility stresses at grain boundaries in Ni bicrystalline micropillars analyzed by an anisotropic model and slip activity. Acta Mater. 83, 227-238 (doi: 10.1016/j.actamat.2014.09.033)

Trautwein, A., Gysel, W., 1982. Influence of Long-Time Aging of CF8 and CF8M Cast Steel at Temperatures Between 300 and 500°C on Impact Toughness and Structural Properties. In

Stainless Steel Castings, pages 165–165–25. ASTM International, 100 Barr Harbor Drive, PO Box C700, West Conshohocken, PA 19428-2959 (doi: 10.1520/STP28441S).

Tsekpuia, E., 2022. Développement et implémentation numérique d'un modèle d'homogénéisation élastoviscoplastique à base microstructurale pour des aciers inoxydables austénito-ferritiques. PhD thesis. Université de Lorraine.

Verhaeghe, B., Bréchet, Y., Louchet, F., Massoud, J.P., Touzeau, D., 1996. Internal stresses in an austenoferritic duplex stainless steel. Phys. Stat. Sol. (a) 153, 47-56 (doi: doi.org/10.1002/pssa.2211530104)

Verhaeghe, B., Louchet, F., Bréchet, Y., Massoud, J.-P., 1997. Damage and rupture mechanisms in an austenoferritic duplex steel. Acta Mater 45(5):1811-1819 (doi: 10.1016/S1359-6454(96)00330-8)

Wang, H., Wu, P.D., Tomé, C.N., Huang, Y., 2010. A finite strain elastic-viscoplastic self-consistent model for polycrystalline materials. J. Mech. Phys. Solids 58, 594-612 (doi: 10.1016/j.jmps.2010.01.004)

Wang, H., Clausen, B., Capolungo, L., Beyerlein, I.J., Wang, J., Tomé, C.N., 2016. Stress and strain relaxation in magnesium AZ31 rolled plate: In-situ neutron measurement and elastic viscoplastic polycrystal modeling. Int. J. Plast. 79, 275-292 (doi: 10.1016/j.ijplas.2015.07.004)

Wang, J., Zecevic, M., Knezevic, M., Beyerlein, I. J., 2020. Polycrystal plasticity modeling for load reversals in commercially pure titanium. International Journal of Plasticity 125, 294-313 (doi: 10.1016/j.ijplas.2019.09.013)

Weng, G.J., 1990. The overall elastoplastic stress-strain relations of dual-phase metals. J. Mech. Phys. Solids 38, 419-441 (doi: 10.1016/0022-5096(90)90007-Q)

Wu, L., Adam, L., Doghri, I., Noels, L., 2017. An incremental-secant mean field homogenization method with second statistical moments for elasto-viscoplastic composite materials. Mech. Mater. 114, 180-200 (doi: 10.1016/j.mechmat.2017.08.006)

Zecevic, M., Lebensohn, R. A., 2020. New robust self-consistent homogenization schemes of elasto-viscoplastic polycrystals. Int. J. Solids Struct. 202, 434-453 (doi:10.1016/j.ijsolstr.2020.05.032)